ph-coding

Predictive Haptic COding Devices In Next Generation interfaces

Grant agreement#: 829186 H2020 FET Open

Start date: 2019-01-01 End date: 2021-12-31

Deliverable reporting document

Deliverable no: 4.2	Lead beneficiary: ICL	WP: WP4
Deliverable name: Predictive coding model	Type: Report	Dissemination level: CO
Due Delivery date: 2020-06-30		Date delivered: 2021-01-01

Deliverable text: This deliverable reports predictive coding models developed from the behaviours observed in experiments with humans subjects, and used to enhance the sensory abilities of robotic systems. The predictive coding concept is first described in chapter 1. Chapter 2 then describes basic aspects of haptic sensing and the adaptation of the body's properties to improve environment perception revealed in human behavioural experiments. Chapter 3 develops a predictive coding framework for robotic haptic exploration, which is composed of a sensory system, a motion planner, an adaptive controller, and a dynamic memory of the objects' model. Simulations and initial tests with our robotic testbed were carried out to validate the developed algorithm.

http://www.ph-coding.eu

Contents

Summary

According to predictive coding theory, the human brain is constantly generating and updating a mental model of the environment. It uses this model to generate actions and predictions of sensory input that are compared to the actual sensory input. Arguably, using a predictive coding approach to design robot controllers can help them make sense of the various sensory signals available, while dealing with their inherent limitations in performance, delay etc. This is the approach we are using in PH-CODING, in which the development of a framework for haptic sensing and exploration is rooted in behavioural studies with humans. We focus on the mechanical interaction aspects often neglected in previous haptic research.

Deliverable D4.2 is part of workpackage 4 in which predictive coding models are developed and implemented into the haptic explorative platform that was demonstrated in D4.1. The proposed predictive coding framework for haptic exploration in this deliverable and the sensorised soft tactile s-skin from WP3 will be integrated and implemented into the robotic haptic exploration interface with distributed tactile sensing. It will support the development of active haptic interfaces and remote human haptic interaction interfaces in WP5. There is a 6-months delay relative to the proposal plan, due to the slow administrative process to hire suitable manpower initially and the limited lab access granted during the covid period.

Adaptive haptic sensing

This deliverable reports two advances in haptics research. First, Chapter 2 presents basic aspects of haptic sensing and the adaptation of the body's properties to improve environment perception. While it is known that the nervous system can modify the body's stiffness by selective cocontraction in order to shape the mechanical interaction with the environment, little is known of how this influences haptic perception. For instance, when we attempt helping our child learn to ride a bicycle, how do we control our muscles to better sense their movement so that we can best guide them?

In Section 2.1, by carrying out a behavioural study with human subjects interacting with a robotic interface and a visual environment, we show that the central nervous system can voluntarily adapt muscle cocontraction to increase haptic sensitivity. Participants tracked a randomly moving noisy visual target while being physically guided by a virtual elastic band whose strength was controlled by the participant's cocontraction. They learned to increase cocontraction under visual noise and decreased it when the guidance was incongruent.

Section 2.2 then studies if and how two subjects connected by a virtual elastic band modulate their muscle cocontraction when they track the same visual target. By varying the visual noise around the target, we can analyse how the subjects changes their muscle activation in function of their own skill and the partner's skill. The results first show how the noise in both partners affect the tracking performance. Second, they reveal that the subjects decrease muscle cocontraction with their own visual noise, and tend to increase cocontraction with increasing visual noise in the partner's target.

Section 2.3 develops a computational model to understand how humans adapt the motor commands in presence of visual and haptic noise. We demonstrate that a model where humans modulate muscle cocontraction to minimise the prediction error and energy, can predict all the experimental observations and explain the results better than alternative models based on error minimisation. This optimal information and energy (OIE) model is expressed as an algorithm that can be implemented on a robotic system, promising robots that can extract maximal information from the interaction with their environment and robotic interfaces that adapt to best support the human operator.

Framework for robotic haptic exploration

Second, Chapter 3 develops a predictive coding framework for robotic haptic exploration, which is composed of a sensory system, a motion planner, an adaptive controller and a dynamic memory of the objects' model. Simulations and initial tests with our robotic testbed were carried out to validate the developed algorithm. These techniques will now be integrated and systematically tested in future experiments.

We developed a sensory system in Section 3.2 that can recognise objects with tactile sensory information acquired during tapping experiments. The analysis of the interaction force and vibration data indicates that the peak force and vibration magnitude can be used to distinguish hard and soft objects. A Naive Bayes classifier is used and trained with data from tapping at different

speeds. The initial results show that prediction accuracy increases with the tapping speed. Furthermore, considering additionally the peak values in six frequency ranges between 0 to 500 Hz from the FFT of the vibration signal yield a high objects' recognition accuracy rate of over 94%.

A motion planner was developed in Section 3.3 to select the optimal exploration action in order to identify the object that the robot is interacting with. We have collected sensory data from the actions of tapping, sliding and pressing with different conditions of 10 objects to form a database. Simulations showed that by selecting the action that maximises the mutual information gain between an action and observations, the robot could select the most suitable action and improve the recognition rate.

An adaptive controller was developed in Section 3.4 to accurately estimate the object viscoelasticity through indentation of its surface. A Kalman filter was used to filter the sensory and motor noise, while the viscoelastic parameters are computed by gradient descent minimisation of the interaction force prediction error. Simulations yielded accurate identification performance, which could help identify objects more precisely.

We present in Section 3.5 a memory to handle the storing of haptic information on different objects, so that they can be recognised, new objects can be added, and objects with similar features are automatically grouped. This is done by considering the initial rough objects' properties estimation from the sensory system and actions selected by the motion planner. Furthermore, the fine estimation of the object's viscoelasticity enables us to test an object selection, and add that new object to the memory if it cannot be attributed to any existing one. This method has been tested in simulations with 10 objects that became automatically part of the memory.

This conceptual framework for predictive coding haptic exploration will be further developed and used from the following perspectives: 1) Extend the motion planner to work with multiple sensors in order to increase the prediction rate; 2) Implement the adaptive controller and relate it more closely with predictive coding, for example use gain scheduling control for the predicted object; 3) complete the dynamic objects' memory with e.g. adaptation to sensory properties and data reduction; 4) Implement, integrate and systematically test this framework on the robotic testbed.

Chapter 1

Predictive coding framework for haptic interaction in humans and robots

1.1 Predictive coding concept

Humans use haptic exploration to interact with their environment, where tactile information is used to recognise object's shapes and mechanical properties. However, it is still challenging for robots to carry out haptic exploration smoothly and recognise objects efficiently, especially in an unstructured environment with soft materials and different textures, due to inherent sensor and motor noise, and delay in sensory signal processing. Using a predictive coding framework to carry out haptic exploration could enhance robot's capability in making it robust and versatile, by learning to prepare an action based on the expectation of sensory information. This means that the robot will be able to use sensory information in real time in order to check whether the expectations are correct and react quickly.

PH-CODING is developing a predictive coding framework combining a sensory system for object recognition and a motor control system for adaptive haptic exploration. This will enable to integrate multiple sensory modalities, optimise sensing, and identify various objects' properties. A robotic explorative system equipped with multiple tactile sensors is being developed to gather necessary tactile information from objects with different interactions and establish a database.

In general, *predictive coding* attempts to make sense of the interaction with the environment by minimising prediction error. A *forward model* uses the motor commands to generate related predictions of sensory inputs, which are compared to actual sensory inputs, and used to update this model of the sensorimotor system and environment. Importantly, both motor and sensing can be adapted. Furthermore, while most existing haptics in robotics concern geometry, but not mechanics critical to soft interactions, the effect of mechanical interactions is at the core of PH-CODING.

In contrast to traditional "bottom-up" approaches to sensing from specific features to building up perception, predictive coding promotes a "top-down" approach relying on prediction error computation. Heterogeneous sensor signals are considered and integrated. In humans this includes vision, muscle spindles, Golgi tendon organs, various skin sensors with different e.g. frequency sensitivity, temperature sensors. For robots, this includes cameras, joint encoders, joint and endpoint force sensors, accelerometers measuring structural vibrations, electronic skin sensors with different sensitivity, temperature sensors, magnetic sensors, etc.

1.2 Adaptive haptic sensing

Humans are endowed with various sensors to interpret the environment and predict the interaction with the environment in a predictive coding interpretation. Of the sensing modalities, haptics, the synthesis of touch and proprioception [1], plays an important role during physicals interaction. In walking down a dimly lit flight of curved steps we instinctively reach out the handrail, that will guide our movement by providing haptic information about the steps direction. The guidance provided by the handrail becomes stronger when the arm is stiffened through muscle cocontraction [2], but how the body's stiffness influences the haptic percept is unclear.

Could the NS adapt the limbs' viscoelasticity by cocontracting muscles in order to improve haptic perception? Examples of such *adaptive sensing* include the pupil's dilation to improve visual sensitivity, and the adaptation of γ-motorneuron's influence on muscle spindle sensitivity to optimise proprioception [3]. In both of these most basic cases of predictive coding, sensing can be studied independently from motor actions. In contrast, haptic sensing, synthesizing information from sensors in the skin, muscles and tendons during contact with the environment, cannot be separated from the mechanical interaction. This makes it challenging to investigate the haptic percept and

dissociate it from the mechanical effect of adapting the limb's viscoelasticity. Furthermore, it is not known how the NS adapts the limb's viscoelasticity to plan motion when information from other sensory modalities like vision is available.

To investigate whether the NS can actively control the viscoelasticity of a limb to improve the haptic percept, we first observed how subjects used wrist flexion and extension to track a moving target to which they were physically coupled by an elastic band. Second, we investigated if and how mechanically connected individuals carrying out a common tasks modulate muscle cocontraction. Third we developed a computational model of the resulting adaptation of mechanical impedance, which can be used to predict the human muscle adaptation and to develop adaptive haptic sensing in robots. This experiments and computational modeling of this basic predictive coding mechanism are described in Chapter 2.

1.3 Haptic exploration in humans

In the predictive coding framework [4, 5], sensory systems and motor control processes are both required to deal with unknown environments during haptic exploration. They are tightly related and interacted together to optimise haptic information as shown in figure 1. An agent interacts with the environments through its body to gain information [6]. For instance, humans use their fingers to squeeze objects, scan and tap on their surfaces to extract their properties such as geometry and stiffness, by analyzing information from many sensory receptors located beneath the skin [7]. The so obtained haptic information is used to compare with predictions of haptic inputs from a forward model in the brain. Prediction errors are computed and used to update the forward model. Meanwhile, motor control signals, which are also influenced by the prediction errors, are used to execute actions or adjust body properties to compensate misleading haptic information, resulting in behaviour adaptations [8]. These adaptions will continue until the prediction errors are minimised.

According to the predictive coding framework, the adaption of behaviours is essential to minimise the prediction errors, i.e. carry out expected actions. For example, when humans need to identify the stiffness of an unknown's object during palpation with blindfold, they would not palpate on the object's surface with fixed postures. They constantly change the pose, scanning speed and direction to gather necessary haptic information to estimate the

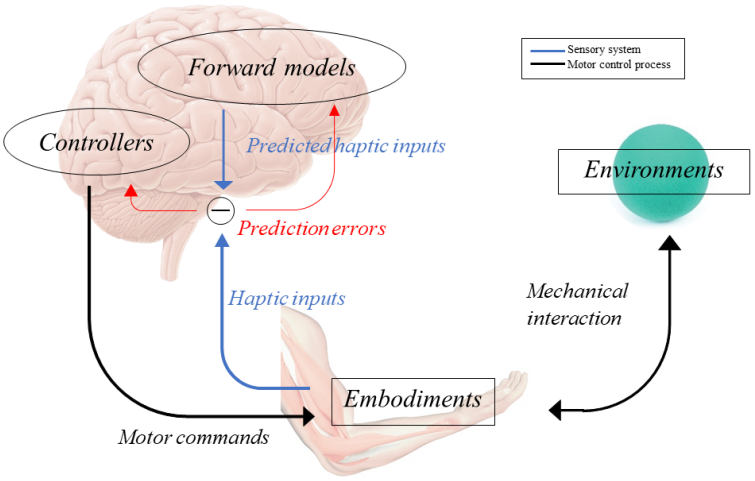

Figure 1: Diagram of haptic exploration in predictive coding framework. Humans interact with an environment through their embodiment. Actual haptic inputs comprising tactile information from interaction with the environment and proprioceptive information are passed to the brain to compare with predictive sensory information generated by the forward models. Consequently, prediction errors are formed. The prediction errors can be minimised by iteratively updating forward model with the past prediction errors, and changing actions to reduce the difference between predicted sensory inputs and the measure ones. When the prediction errors are minimised, the most likely causes of sensory inputs are generated.

object's property, e.g. stiffness. Besides, the adaption of behaviour, especially in stiffness, also helps humans to maintain stability when interacting with unstable environments, by preparing and shaping the interaction with environments, as in turn information gain could be improved [9]. For these benefits, the ability of humans to control viscoelasticity has caught a lot of attention from the robotics research community to apply this approach in robots [10]. However, the role of adaptive behaviours in the robotics community seems to mainly focus on the control aspects, not on the haptic sensing and exploration aspects, in particular for tactile perception.

1.4 Haptic exploration in robots

Features such as shape, material properties and position of objects are critical for robots to properly interact with the surrounding. Vision has been a popular approach to guess object's material properties [11, 12, 13]. However, methods based on vision can only identify objects using previously known environment features, and cannot estimate the environment's mechanical properties. Besides, the computational cost of image processing is relatively high. Therefore, haptic exploration has gained attentions from researchers in the past few decades for robots to gather essential environment features. In addition, because of tremendous progresses in the development of sensors, haptics may help improve the capabilities of robot to identify the environments at a level comparable to humans [14].

Methods that are normally applied for haptic exploration in robots can be distinguished into passive and active exploration. In *passive exploration*, robots equipped with multiple sensory modalities interact with objects intentionally to obtain haptic information. Many studies have shown that obtained information such as interaction forces and vibrations can help estimate object's properties such as textures, roughness and compliance [15, 16, 17]. Janine et al. investigated statistical methods, robot motions and classification methods to determine the best approach to recognise objects, that could achieve maximally 97.6 % of accurate resolution [18]. However, the robot's actions in passive exploration are not influenced by the haptic information gained during movement. Previous studies have shown that passive exploration gives poor results in object's classifications compared to active exploration when a robot contacts an object that leads to an unstable interaction [19, 20].

In *active exploration*, haptic information is used to influence robot's action commands in order to enhance haptic sensing. A series of developments of active exploration algorithms have shown that using haptic information as a feedback modality for robots to re-position themselves could improve robustness and accuracy rates in classifications compared to passive exploration, even if the robot moves randomly [19, 20, 21, 22]. However, many previous works in active exploration have been carried out by exploring only rigid objects with constant surface's texture where the forces were used to locate the contacts in shape estimations [23, 24, 25]. To perform haptic exploration like humans do, especially in environments with various characteristics e.g. soft objects, the consideration of object's features apart from shapes such as mechanical properties as well as spontaneous adaptive capabilities are required to maintain stability during the exploration. The lack of both abilities

will lead to exploration failures in objects with varying geometry and textures because of unstable interaction caused by an improper controllers and insufficient information.

Impedance control has been extensively developed for contact interaction in robotics [10], and is widely used in many applications such as adaptive prosthetic limbs [26] and adaptive exoskeletons [27, 28]. However, there have been few studies on haptic exploration. Recently, Li et al.[29] have developed a controller that can adapt feedforward force, impedance and reference trajectory based on robot's position information. Demonstration examples showed that the robot can maintain stability during haptic exploration in various kinds of environment, including rigid and soft surfaces. Sornkran et al. investigated the role of impedance control in robotic embodied perception [30] and used the obtained knowledge to develop a nodule's depth estimation robot [31]. Their results suggested that nodule's depth estimation accuracy can be enhanced by tuning robot's impedance. Therefore, it appears that impedance control can be used as a basic control strategy for haptic exploration in robots. However, the above previous works did not integrate local haptic information from objects which is also critical for haptic exploration.

A further investigation and development of tactile modality integration is required to improve its capabilities and harness it to widen the range of unknown environments with various characteristics that can be interacted with. To our knowledge, a method that combines multiple tactile sensory information and adaptive impedance control in predictive coding framework enhancing haptic sensing and enabling robots to explore wide ranges of environment is lacking. The framework to develop such haptic exploration with robot is described in Chapter 3.

Chapter 2

Adaptation of haptic sensing

2.1 Humans can adapt haptic sensing to visual and haptic perturbations

While the nervous system can modify the body's stiffness by selective co-contraction to shape the mechanical interaction with the environment [32], little is known of how this influences haptic perception. There is evidence suggesting that the central nervous system (CNS) can alter the sensitivity of its sensors, but the possibility to regulate haptic sensitivity have yet to be addressed. Haptics is challenging to investigate as the percept (the interaction force) is entwined with the mechanical guidance. Here, we disentangle the mechanical guidance from the haptic percept to study the brain's capacity to regulate its haptic sensitivity, and uncover the mechanism behind its regulation.

To this end, we developed a new paradigm wherein participants used the cocontraction of a flexor-extensor pair of wrist muscle to control the strength of the elastic guidance while following a randomly moving target trajectory (Fig.1A). A control experiment was devised to isolate the mechanical effect of the elastic guidance, enabling us to study how the haptic percept changed with the wrist's stiffness. Using this paradigm, we could systematically investigate whether and how the CNS adapts the body's stiffness in response to visual and haptic noise.

Methods

Experimental apparatus The experiments described below were approved by the Joint Research Compliance Office at Imperial College London. 59 participants without known sensorimotor impairments, aged 21–36 years, including 22 females, were recruited to take part in one of the three main experiments and the two control experiments. Each participant gave written informed consent prior to participation. 56/59 participants were right-handed and 3/59 left-handed, as was assessed using the Edinburgh Handedness Inventory [33].

Each participant was seated comfortably on a height-adjustable chair next to the Hi5 robotic interface [34], and held a handle with their dominant wrist. A

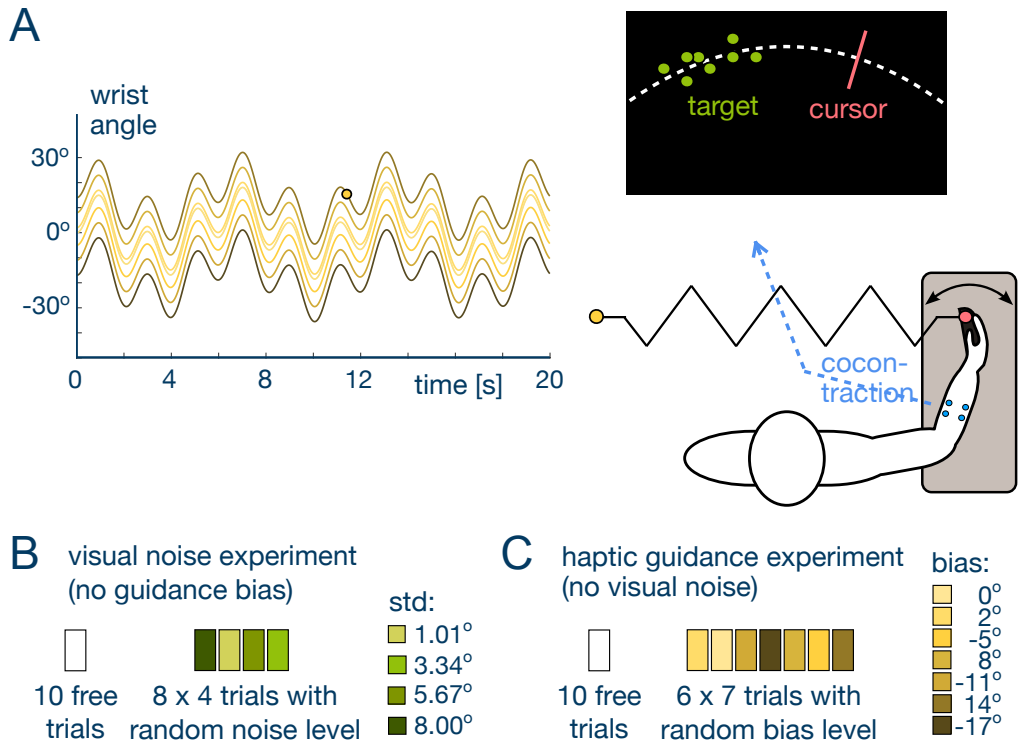

Figure 1: Schematic of the experimental task and protocol. (A) Subjects tracked a randomly moving target with their wrist flexion-extension movement while being guided by a virtual elastic band. The strength of the guidance increased with the cocontraction of a flexor-extensor muscle pair estimated from their myoelectrical activity. (B) Protocol of the experiment to study the effect of visual noise on the cocontraction. (C) Protocol to examine the effect of bias in the guidance trajectory with respect to the target on the cocontraction.

screen placed in front of the participant provided visual feedback of the task with a cursor indicating the current wrist position (Fig.1A). The Hi5 handle is connected to a current-controlled DC motor (MSS8, Mavilor) that can exert torques of up to 15 Nm, and was equipped with a differential encoder (RI 58-O, Hengstler) to measure the wrist angle and a force sensor (TRT-100, Transducer Technologies) to measure the exerted torque in the range [0,11.29] Nm. The Hi5 system is controlled at 1kHz using Labview Real-Time v14.0 (National Instruments) and a data acquisition board (DAQ-PCI-6221, National Instruments), while data was recorded at 100 Hz.

The activation of two antagonist wrist muscles, the flexor carpi radialis (FCR) and extensor carpi radialis longus (ECRL), were recorded with surface electrodes using a medically certified non-invasive electromyography system (g.LADYBird + g.GAMMABox + g.BSamp, g.Tec). The raw muscle activity was high-pass filtered at 20 Hz, rectified, then low-pass filtered at 5 Hz. The filtering process yielding the filtered muscle activity was in both cases a second-order Butterworth filter.

Cocontraction computation Every experiment started with an *EMG normalization* to map the raw muscle activity (in mV) to a corresponding torque value (in Nm). The subject placed their wrist in the most comfortable middle posture, which was set to 0°. Constrained at that posture, they were then instructed to sequentially (*i*) flex, or extend the wrist to exert a torque, or (*ii*) maximally co-contract in order to keep the wrist position stable during a 3 Hz sinusoidal positional disturbance of 10° amplitude. Each phase was 4 s long with a 5 s rest period between consecutive contraction phases to avoid fatigue, which was used as a reference activity in the relaxed condition. This was repeated four times at flexion/extension torque levels {1,2,3,4} Nm and {-1,-2,-3,-4} Nm, respectively. For each subject, the recorded muscle activity was linearly regressed against the torque values to estimate the relationship between them. The torque of the flexor muscle was modelled from the filtered EMG signal u_f as

$$\tau_f(t) = \alpha_0\, u_f(t) + \alpha_1\,, \quad \alpha_0, \alpha_1 > 0\,, \tag{2.1}$$

and similarly for the torque of the extensor muscle τ_e. *Muscle cocontraction* was then computed as

$$u(t) \equiv \min\{\tau_f(t), \tau_e(t)\}\,. \tag{2.2}$$

The average cocontraction over all participants (as shown in Figs.2B,D) was

computed from each participant's normalised cocontraction, calculated as

$$u_n \equiv \frac{\overline{u} - \overline{u}_{min}}{\overline{u}_{max} - \overline{u}_{min}}\,, \quad \overline{u} \equiv \frac{1}{T}\int_0^T u(t)\,dt\,, \quad T = 20\,s \tag{2.3}$$

with $\overline{u}_{min}$ and $\overline{u}_{max}$ the minimum and maximum of the means of all trials of the specific participant.

Tracking with visual and haptic feedback In the three main experiments of sections D-F, subjects were required to track a *visual target* (in degrees) moving with

$$q^*(t) \equiv 18.5\,\sin\!\left(\frac{\pi t}{1.547}\right)\,\sin\!\left(\frac{\pi t}{2.875}\right), \quad 0 \le t \le 20\,s \tag{2.4}$$

using flexion-extension movements (Fig.1A). After each 20 s long trial, the target disappeared and the participant was required to place the hand on the starting position at the center of the screen. The next trial then started after a 5 s rest period and a 3 s countdown. Each subject was instructed to take small breaks when feeling (mental or physical) fatigue during the course of the experiment. The *tracking error*

$$e \equiv \left(\frac{1}{T}\int_0^T [q^*(t) - q(t)]^2\,dt\right)^{\frac{1}{2}}, \quad T \equiv 20\,s \tag{2.5}$$

was displayed at the end of each trial, where $q(t)$ is the angle of the wrist.

The tracking task consisted of a *free phase* (in which no interaction torque was exerted on the wrist) to get the subject accustomed with the Hi5 interface, followed by an *interaction phase* in which the subject's wrist position was connected to a *haptic reference trajectory* $q_h(t)$ with an elastic force

$$\tau(t) = \kappa(t)\,[q_h(t) - q(t)]\,, \quad \kappa(t) \equiv \frac{u(t)}{8} \tag{2.6}$$

where the connection stiffness $\kappa < 0.25\,\mathrm{Nm}\,/^\circ$ linearly increased with the cocontraction $u(t)$.

Subjects were informed of the possibility to regulate the coupling stiffness by co-contracting or relaxing wrist's muscles, and of the transition of free trials to interaction a phase of interaction trials. They were instructed not to resist large torques provided by the motor.

Visual noise experiment In this experiment $q_h \equiv q^*$ thus there was no haptic noise. 15 right-handed subjects (7 females, aged 23.46±2.39 years old) carried out a visual noise experiment. The target trajectory was displayed on the screen either as a 8 mm diameter circle or as a "cloud" of eight normally distributed dots around the target (Fig.1A), depending on the experimental condition. The cloud of dots were defined by three parameters, randomly picked from independent Gaussian distributions: the vertical distance to the target position $\eta \in \mathrm{N}(0, 15\,\mathrm{mm})$, the angular distance to the target position $\eta_q \in \mathrm{N}(0, 0{<}\sigma_v{<}8.00°)$, and the angular velocity $\eta_{\dot{q}} \in \mathrm{N}(0, 4°/\mathrm{s})$. The amplitude of visual noise was controlled by the angular distance deviation, while both the vertical and the angular velocity deviations were kept constant. The dots were updated sequentially so that each dot was replaced every 100 ms. The experimental protocol consisted of 10 free trials followed by 32 interaction trials split into 8 blocks. The 4 trials of each block used a different value of $\sigma_v \in \{1.01°, 3.34°, 5.67°, 8.00°\}$ presented in a random order in each block (Fig.1B). We assume that the ordering of the blocks has no effect.

Haptic guidance experiment In this experiment the target was a 8 cm diameter disk, and the elastic guidance trajectory was biased by δ relative to the target trajectory:

$$q_h(t) \;=\; q^*(t) + \delta\,. \tag{2.7}$$

Another 13 participants (4 females, 12 right-handed, aged 23.53±3.03 years old), carried out a haptic noise experiment. The experiment consisted of 52 trials with 10 free trials followed by 42 interaction trials subdivided into 6 blocks. The 7 trials of each block had a different $\delta \in \{0°, 2°, -5°, 8°, -11°, 14°, -17°\}$, where these bias conditions were presented in a random order in each block (Fig.1C).

Visual and haptic bias experiment A third experiment with both visual and haptic noise was carried out with 15 subjects (aged 25.06±2.12 years old, with 5 females, 14 right-handed). The protocol consisted of 40 trials with 8 free trials, followed by a 32 interaction trials in 8 blocks of 4 trials. In these 4 trials, the participant experienced different combinations of the guidance bias and visual noise $(\delta, \sigma_v) \in \{(1.5°, 0°), (1.5°, 6.7°), (8.5°, 0°), (8.5°, 6.7°)\}$, presented in a random order in each block.

Experimental results

We first examined the results from the visual noise tracking experiment wherein increasing amounts of visual noise were imposed on the target to

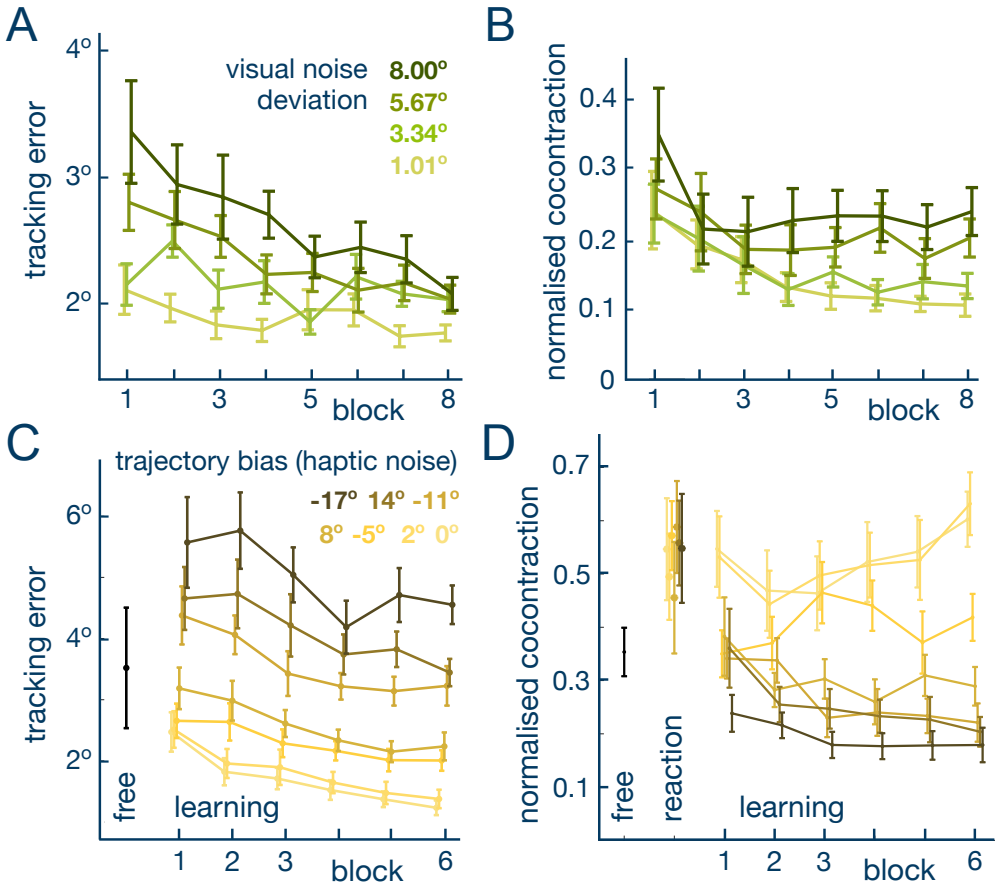

Figure 2: Tracking error and muscle cocontraction adapted with training. The figures shows the mean values with standard error bar over all trials of each subject in the corresponding block. (A) The population mean tracking error and the associated variability decreased with trials for every level of visual noise. (B) The normalised cocontraction was initially large in the first block of trials for all visual noise conditions and decreased with practise. The level to which the cocontraction converged was dependent on the visual noise imposed on the target. (C) In the haptic bias experiment the tracking error magnitude over one trial decreased with training, with higher error when the haptic bias was greater. (D) The initial cocontraction was comparable for all haptic bias levels, but participants gradually learned to increase the elastic stiffness with smaller haptic bias and decrease it with large haptic bias.

which the participants were elastically guided (Fig. 1B). The strength of the elastic guidance was controlled by the participants themselves through the cocontraction of their wrist. Figs. 2A and 2B show the square root of square error over a trial or *tracking error* and the mean cocontraction as a function of the block number, separately for each level of visual noise.

The tracking error magnitude was large but gradually decreased over blocks (Fig. 2A). The effect of training was measured by comparing the error in the first and last blocks. A two-way repeated measures ANOVA showed that both the visual noise ($p<0.001$, $F(3,40)=8.67$) and the training ($p=0.002$, $F(1,12)=14.34$) had a significant influence on the error. Post-hoc comparisons using Tukey's HSD confirmed a decrease of tracking error with training for the two higher levels of visual noise ($p=0.027$ and $p<0.001$ respectively).

We then looked at how the mean cocontraction measured over a whole trial depended on the visual noise and the block number. The cocontraction was normalized for comparisons between participants. A two-way repeated measures ANOVA revealed a significant effect of both the visual noise level ($p<0.001$, $F(3,40)=8.3$) and training ($p=0.01$, $F(1,12)=8.9$) on the normalized cocontraction. Post-hoc comparisons confirmed that the normalized cocontraction in the first block was comparable across all visual noise levels, but different between the lowest and highest visual noise levels in the last block ($p=0.02$). The normalized cocontraction tended to decrease over blocks by a larger amount when the visual noise was lower. This yielded a normalized cocontraction in the final three blocks that increased monotonically with the level of visual noise (slope$=0.019>0$, $p<0.001$, t-test on the last three blocks). This suggests that the CNS adapts the body's stiffness to modify the haptic guidance in response to visual noise on the target.

Next, we examined the results from a second tracking experiment where the target was displayed without visual noise but the guidance trajectory was shifted from the target by increasing amounts (Fig. 1A,C). The tracking error tended to increase with the size of the guidance bias as shown in Fig. 2C. A two-way repeated measures ANOVA revealed a significant influence of the guidance bias ($p<0.001$, $F(6,71)=28.44$) and the training ($p<0.001$, $F(1,12)=18.96$) on the tracking error. Post-hoc comparisons revealed a significant decline in the error between the first and the last blocks across all bias levels. The error was also higher with greater bias ($p<0.001$ comparing highest and lowest bias).

The improvement in the tracking error with guidance bias was also accompanied by an adaptation of the wrist's cocontraction (Fig. 2D). We first

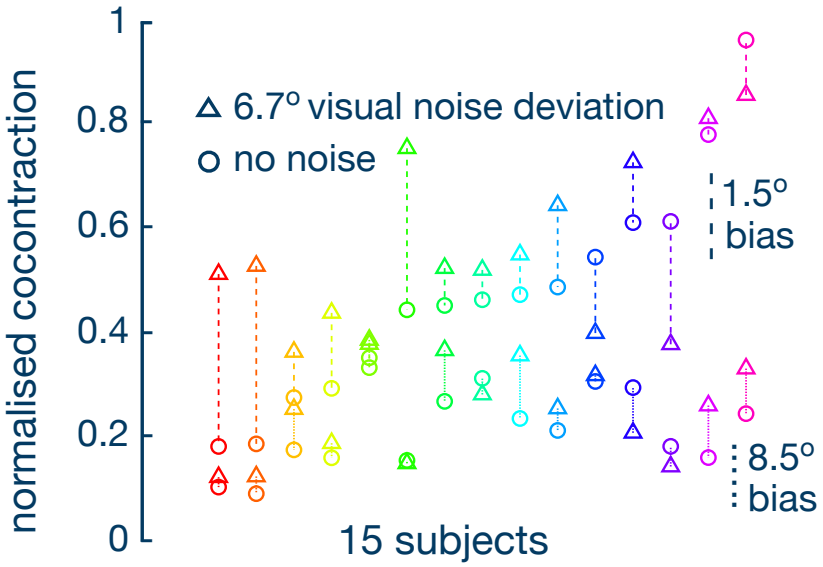

Figure 3: How cocontraction changes with visual noise and haptic bias, for each of 15 subjects. In most subjects, cocontraction increased with visual noise while the larger haptic bias led to decreasing it.

analyzed how the participants react to the different levels of bias by measuring the mean normalized cocontraction in the first 200 ms (see Supplementary Figure 4). Participants initially reacted to the guidance by cocontracting greatly regardless of the bias ($p=0.78$, $F(6,71)=0.44$, repeated measures ANOVA on the different bias level conditions with Greenhouse-Geisser correction). However, the normalized cocontraction tended to decrease thereafter on trials with a large bias, and increased on select trials wherein the bias was small, as if the CNS was modulating the cocontraction in response to the congruency between the target and the guidance (Fig. 2D). A one-way repeated measures ANOVA confirmed that larger bias was associated with smaller cocontraction in the last block ($p<0.001$, $F(1,12)=153.09$). It appears that the CNS also modulated the body's stiffness in response to the quality of the haptic guidance.

The participants in both the visual noise and the guidance experiments improved their tracking performance with training, and modified the body's stiffness depending on the level of the visual noise and the amount of bias on the guidance trajectory. Increasing visual noise induced participants to increase their concontraction, in line with previous studies on learning in unpredictable dynamic environments [32, 35]. However, large haptic noise caused a reduction in the cocontraction, in contrast to the effect observed in

unpredictable dynamic environments [32, 35]. The subjects were also able to modulate cocontraction in presence of both visual and haptic noise as can be seen in Fig.3. The CNS had seemingly learned to modify the body's stiffness in accordance with its effect on the tracking performance.

Discussion

Human motor control has revealed how the CNS controls the body's stiffness to shape the mechanical interaction with the environment [36, 37, 32], and morphological computation has analysed how the biomechanical design in animals facilitates their functions [38, 39]. Different from these motor and morphological adaptations, our results provide the first evidence that the CNS can actively control the body's stiffness *to regulate its haptic sensitivity*. The association of sensory modalities and their stochastically optimal integration has been reported in numerous studies [40, 41], whereby the reliability of each sensory input was manipulated externally by the experimenter. In contrast, the haptic sensitivity in our experiment was actively controlled by the participants themselves through the strength of the guidance.

While previous studies have provided qualitative evidence of adaptive sensing in humans [3, 42, 43], we could quantify the performance improvement resulting from the reduction in haptic noise as a consequence of greater body stiffness or cocontraction. Importantly, to obtain these results, it was necessary to subtract the mechanical guidance from the haptic percept. The haptic tracking control experiment enabled us to isolate the mechanical effect of the haptic guidance on the tracking performance, and then deduct it to determine how the haptic percept was influenced by the limb's cocontraction. The increase of visuo-haptic accuracy observed in our experiment may also explain why increasing the body's stiffness can speed up the acquisition of internal models of novel dynamics [44].

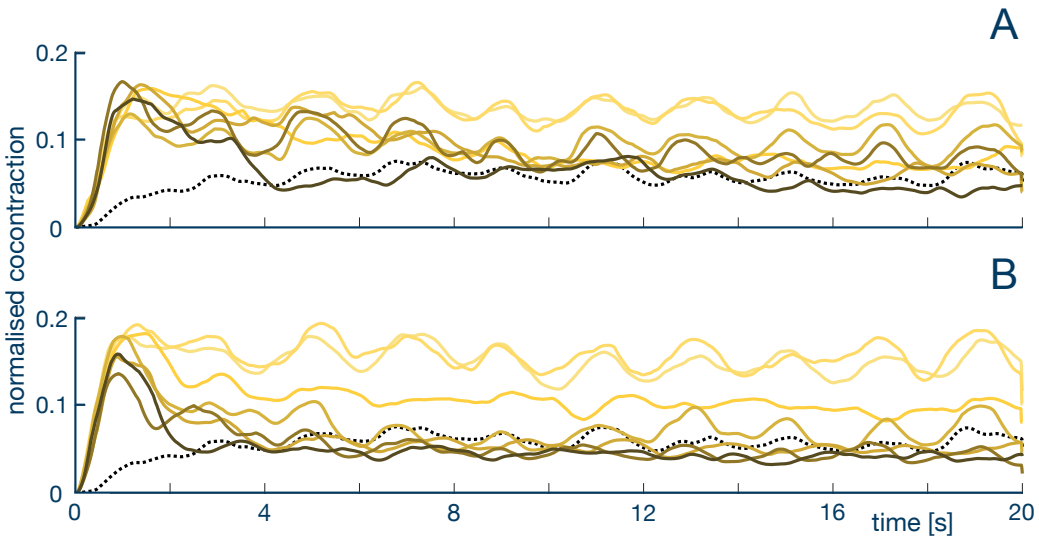

Figure 4: Supplementary Figure: Evolution of normalised cocontraction in the biased guidance experiment. Cocontraction waveforms with different trajectory bias in the first (A) and last (B) blocks. The data exhibits quicker settlement to discite at stable levels of cocontraction for different trajectory biases in last block (2 s vs. 4 s).

2.2 Interacting humans regulate muscle cocontraction to improve visuo-haptic perception

During tango dancing, the arms can be relaxed or kept stiff, but it is unclear how these changes influence the perception of the partner's movements through haptics. While the CNS is known to increase the limb's stiffness through muscle cocontraction to reject force perturbations from unstable environments [2, 32], how this regulation influences haptic sensing is not known. Recent studies have shown that physically connected individuals exchange haptic information to improve their performance [45]. While this haptic communication is influenced by the stiffness of the haptic connection [46], we do not know if humans actively regulate their limb stiffness to better sense the partner's actions.

To address this question, we observed how rigidly connected pairs of subjects or *dyads* tracked a common, randomly moving target using wrist flexion and extension (Fig.5A). While each partner's visual feedback was manipulated to be either sharp or fuzzy, we monitored how each individual adapted the

cocontraction of their wrist. We hypothesized that the cocontraction should be large with a worse partner who disturbs your movement. Accordingly, the cocontraction should be large when one's own visual feedback is sharp and the partner's is fuzzy (sharp-fuzzy condition, shortened to SF), and it should be low when the partner's vision is sharp (sharp-sharp or SS and fuzzy-sharp or FS). We also expected cocontraction to be low in the fuzzy-fuzzy condition (FF) as your own performance is likely to be as bad as the partner's. If a partner's inferior performance induces greater cocontraction, we expected the cocontraction to follow the approximate relationship SF $>$ SS $\approx$ FS $\approx$ FF.

Methods

Participants The experiment was approved by the Joint Research Compliance Office at Imperial College London. 44 participants without known sensorimotor impairments, aged 18–37 years, including 16 females, were recruited. Each participant gave written informed consent prior to participation. 37/44 participants were right-handed and 5/44 left-handed, as was assessed using the Edinburgh Handedness Inventory [33]. The participants carried out the experiment in pairs or *dyads*, with 14 male-male dyads and 8 female-female dyads.

Experimental setup The two participants of a dyad were seated comfortably on height-adjustable chairs, next to the Hi5 dual robotic interface [34], and each partner held one of the handles with their right wrist. A personal screen placed in front of each participant provided them visual feedback of the task with a cursor indicating their own wrist position (Fig.5A). No visual feedback of the partner's position was available as the two participants were separated by a curtain, and they were instructed not to speak to each other during the experiment.

Each Hi5 handle is connected to a current-controlled DC motor (MSS8, Mavilor) that can exert torques of up to 15 Nm, and is equipped with a differential encoder (RI 58-O, Hengstler) to measure the wrist angle and a (TRT-100, Transducer Technologies) sensor to measure the exerted torque in the range [0,11.29] Nm. The two handles are controlled at 1 kHz using Labview Real-Time v14.0 (National Instruments) and a data acquisition board (DAQ-PCI-6221, National Instruments), while the data was recorded at 100 Hz.

By each participant, the activation of two antagonist wrist muscles, the flexor carpi radialis (FCR) and extensor carpi radialis longus (ECRL) were recorded

during the movement. Electromyographic (EMG) signals were measured with surface electrodes using the medically certified g.Tec's g.LADYBird&g.GAMMABox&g.BSamp system. The EMG data was recorded at 100 Hz.

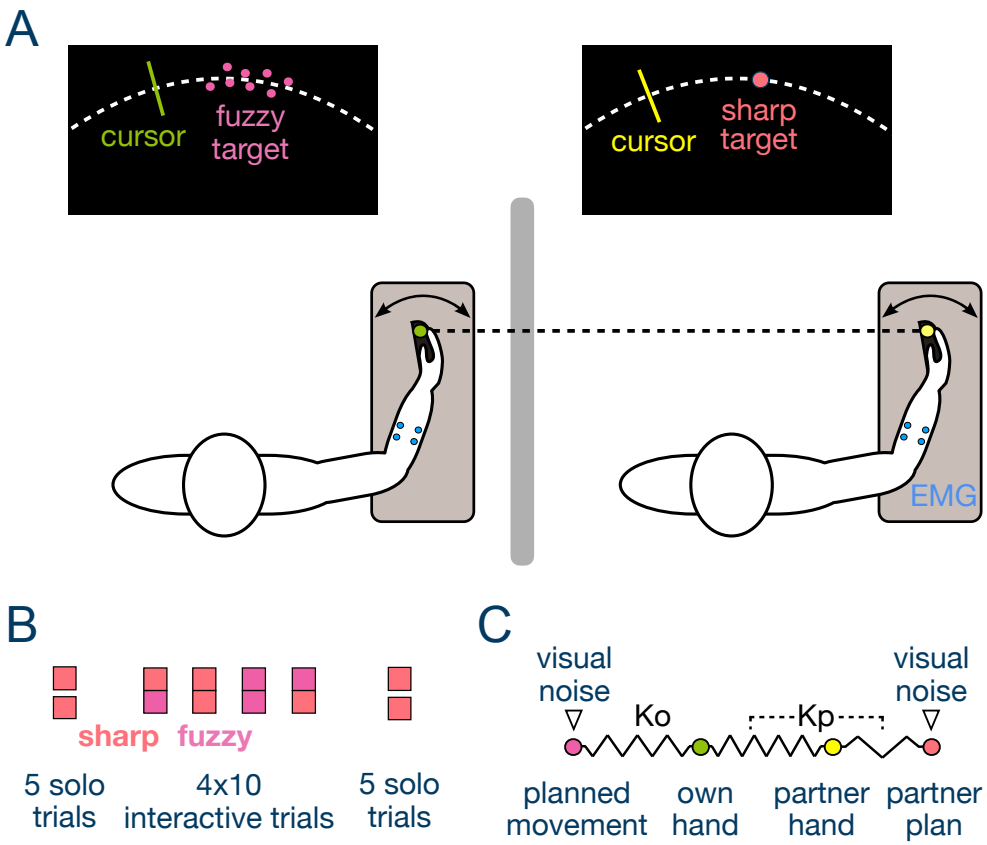

Figure 5: Schematic of the experimental task and modeling. (A) The two partners tracked the same randomly moving target with their wrist flexion-extension movement while being connected with a rigid virtual elastic band. The wrist flexion/extension movement was recorded, as well as the myoelectrical activity of a flexor-extensor muscle pair. (B) Protocol of the experiment to study the effect of visual noise on either partner on performance and cocontraction. (C) Mechanical modeling of the interaction with the partner and with own movement plan. Own and the partner movement plans are affected by their respective visual noise. The interaction with the partner's hand is influenced by the viscoelastic connection to their motion plan modulated by their cocontraction.

Tracking task The two partners were required to track the same *visual target* (in degrees) moving with

$$q^*(t) \equiv 18.5 \sin\left(\frac{\pi\,(t+t_o)}{1.547}\right) \sin\left(\frac{\pi\,(t+t_o)}{2.875}\right), \quad 0 \le t \le 20\,s \tag{2.8}$$

as accurately as possible using flexion-extension movements (Fig.5A). To prevent the participants from learning the target movements, t^* started in each trial from a randomly selected zero $\{t_0 \in [0, 20]\,\mathrm{s} \mid q^*(t_0) \equiv 0\}$ of the multi-sine function. The respective *tracking error*

$$e \equiv \left(\frac{1}{T}\int_0^T [q^*(t) - q(t)]^2\,dt\right)^{\frac{1}{2}}, \quad T \equiv 20\,s \tag{2.9}$$

was displayed at the end of each 20 s long trial.

After each trial, the target disappeared and the participants were required to place their respective cursor on the starting position at the center of the screen. The next trial then started after a 5 s rest period and a 3 s countdown. The initialization of next trial started when both participants placed their wrist on the starting position, so that each participant could take a break at will in between trials, by keeping the cursor away from the center of the screen.

Experimental conditions and protocol

Two kinds of trials were carried out. In *solo trials*, the two partners moved the wrist independently to each other. In *interactive trials*, the partners' wrists were connected by a rigid virtual elastic band producing a torque (in Nm)

$$\tau(t) = 17.2\,[q_p(t) - q_o(t)]\,, \tag{2.10}$$

where q_o and q_p (in radian) denote own and the partner's wrist angles. As the tracking errors of the two partners of a dyad were strongly correlated ($r(20)=0.95$, $p<0.0005$), the average tracking error between them was used in the data analysis.

The interaction trials were carried out under two different visual feedback conditions. In the *sharp condition* the target was displayed as a 8 mm diameter disk. In the *fuzzy condition* the target trajectory was displayed as a "cloud" of eight normally distributed dots around the target. The cloud of dots were defined by three parameters, randomly picked from independent Gaussian distributions: the vertical distance to the target position $\eta \in$

$\mathrm{N}(0, 15\,\mathrm{mm})$, the angular distance to the target position $\eta_q \in \mathrm{N}(0, 4.58°)$, and the angular velocity $\eta_{\dot{q}} \in \mathrm{N}(0, 4.01°/\mathrm{s})$. Each of the eight dots was sequentially replaced every 100 ms.

An EMG calibration (Sec. 2.2) was first carried out to map the raw EMG signal (in mV) to a corresponding torque value (in Nm), so that the activity of each participant's flexor and extensor's can be compared and combined in the data analysis. After this calibration, the participants carried out 5 initial solo trials to learn the tracking task and the interface dynamics. This was followed by 4 blocks of 10 interaction trials, each with one of the different noise conditions {fuzzy(self)-sharp(partner), SF, SS, FF} presented in a random order, followed by 5 control solo trials (Fig.5B). The participants were informed when an experimental condition would be changed but not which condition would be encountered in the next trials.

Muscle activation calibration and cocontraction calculation The participants placed their wrist in the most comfortable middle posture which was set to 0°. Constrained at that posture, they were then instructed to sequentially (*i*) flex, or extend the wrist to exert a torque, or (*ii*) maximally co-contract in order to keep the wrist position stable during a 3 Hz sinusoidal positional disturbance of 10° amplitude. Each phase consisted of 4 s long followed by a 5 s rest period to avoid fatigue. The latter period was used as a reference activity in the relaxed condition. This procedure was repeated four times at flexion/extension torque levels of {1,2,3,4} Nm and {-1,-2,-3,-4} Nm, respectively. For each participant, the recorded muscle activity was then linearly regressed against the torque values to estimate the relationship between them. The raw EMG signal was first high-pass filtered at 20 Hz using a second-order Butterworth filter to remove drifts in the EMG signal. This was then rectified and passed through a low-pass second-order Butterworth filter with a 5 Hz cut-off frequency to obtain the envelope of the EMG activity.

The torque of the flexor muscle could then be modelled from the envelope of the EMG activity u_f as

$$\tau_f(t) = \alpha_0\, u_f(t) + \alpha_1\,, \quad \alpha_0, \alpha_1 > 0\,, \tag{2.11}$$

and similarly for the torque of the extensor muscle τ_e. *Muscle cocontraction* was then computed as

$$u(t) \equiv \min\{\tau_f(t), \tau_e(t)\}\,. \tag{2.12}$$

The average cocontraction over all participants (as shown in Fig.6B) was

computed from each participant's normalised cocontraction, calculated as

$$u_n \equiv \frac{\overline{u} - \overline{u}_{min}}{\overline{u}_{max} - \overline{u}_{min}}\,, \quad \overline{u} \equiv \frac{1}{T}\int_0^T u(t)\,dt\,, \quad T \equiv 20\,s \tag{2.13}$$

with $\overline{u}_{min}$ and $\overline{u}_{max}$ the minimum and maximum of the means of all trials of the specific participant.

Results

To test our hypothesis, 11 dyads carried out a dyadic tracking task wherein the visual performance feedback to each participant in the dyad were independently manipulated to be sharp or fuzzy (see section 2.2), and we studied how the tracking error and the muscle contraction level were affected by each of the noise conditions {FS, FF, FS, SS}. The experiment was carried out as a within-subject design with these four experimental conditions randomly presented in a block of ten trials each. These interaction trials were preceded by five solo trials without interaction with the partner to learn the task, and followed with five solo trials as control.

In order to evaluate the short-term adaptation within each condition, the measurements from the first half and the second half of trials were averaged into two epochs for statistical analyses. The tracking error was analysed per dyad (as the two partners of a dyad were rigidly connected) using a two-way repeated-measures ANOVA with noise conditions {SS, FF, SF $\equiv$ FS} and epoch as the factors. Statistical significance was detected at 5% with Bonferroni correction for all post-hoc comparisons. As muscle cocontraction was modulated by each partner, it was analysed on a participant level wherein the partner's visual noise was perceived as "haptic noise". Thus, a three-way repeated-measures ANOVA with visual noise, haptic noise and Epoch as the factors was used to analyse the cocontraction level.

The tracking error decreased in the initial solo trials (Fig. 6A), and this learning had saturated by the last of the initial solo trials to the same degree as the average of the last solo trials (paired-sample t-test, t(21)=0.354, p=0.73). The analysis of error in the different noise conditions indicated the magnitude of the tracking error depended on the noise level ($F(1,21) = 91.95$, $p<0.001$, $\eta_p^2 = 0.81$). The post-hoc comparisons showed that the tracking error in the mixed noise condition (SF and FS) was greater than in the SS condition ($p<0.001$) and smaller as in the FF condition ($p<0.001$). The tracking error remained at a similar level between the first and the second

epochs (p=0.64), and there was no interaction effect between the noise level and epoch (p=0.17).

As is generally observed during learning [47, 48], the cocontraction level decreased with the epoch (F(1,43)=53.58, p<0.0005, $\eta_p^2 = 0.56$) (Fig.6B). This is consistent with the observations during the adaptation to a force field [49], where the movement error is reduced quickly while the cocontraction adapts at a slower rate. Furthermore, the cocontraction level decreased with the level of own *visual noise* (F(1,43)=85.91, p<0.0005, $\eta_p^2 = 0.67$), while it increased with *haptic noise* resulting from the interaction with the partner (F(1,43) = 5.53, p<0.03, $\eta_p^2 = 0.11$).

The visual noise had a large effect on cocontraction but not haptic noise. Augmenting visual noise decreased the cocontraction by 0.194 when the hap-

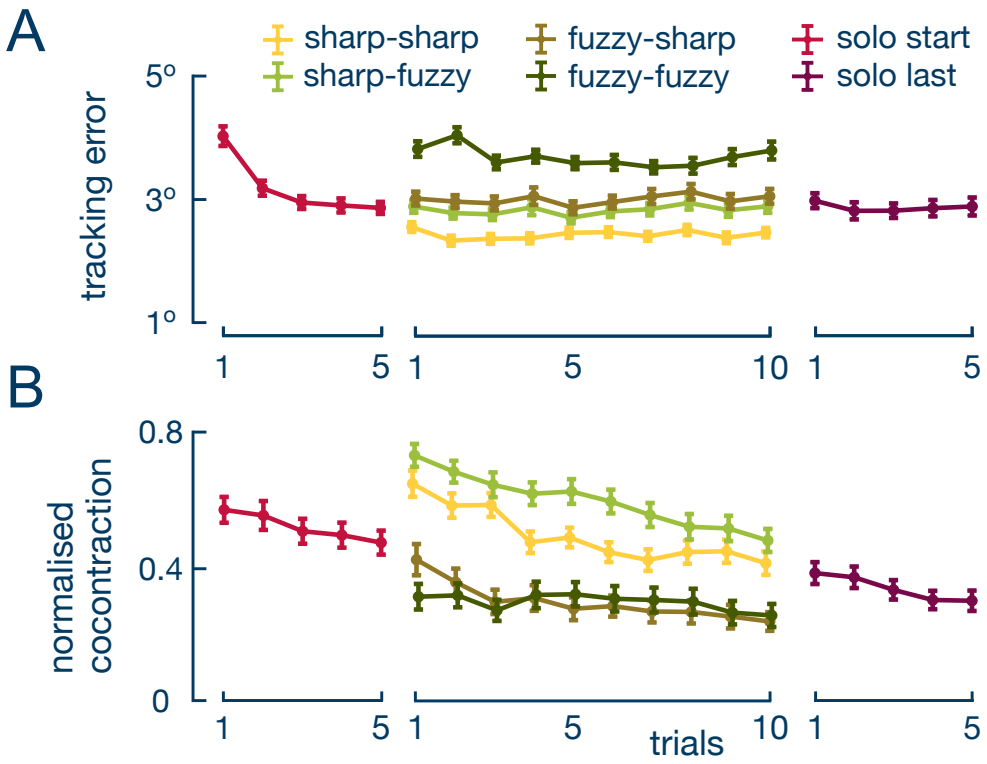

Figure 6: Evolution of performance and cocontraction in different noise conditions. Error bars represent one standard error. A: Group mean tracking error charted as a function of trials. The error saturated in the initial solo trials, and increased with visual and haptic noise. B: The normalized cocontraction as a function of trials. The cocontraction decreased across all noise conditions, while visual noise tended to increase the cocontraction by a larger margin than the haptic noise.

tic noise was low (i.e. FS-SS) and 0.293 when the haptic noise was high (FF-SF), while the cocontraction increased by only 0.100 when haptic noise increased with high visual noise (SS-SF) and 0.001 with low visual noise (FS-FF). The post-hoc comparisons confirmed that all differences between the combinations of the visual and haptic noises were significant with the exception of FS vs. FF ($p = 0.99$). There was an interaction effect between visual noise and epoch ($F(1,43) = 15.65$, $p<0.001$, $\eta_p^2 = 0.27$), and no significant interaction was found between haptic noise and epoch ($p=0.21$). Hence, the decline in the cocontraction occurred at similar rates in all noise conditions.

These results demonstrate that the CNS spontaneously modulates muscle cocontraction with the level of the visual noise on one's own and the partner's target, in agreement with our first hypothesis. However, the observed cocontraction patterns contradict the second hypothesis as it decreased with own visual noise and increased with the haptic noise stemming from the visual noise at the partner. How to explain this discrepancy in reaction to the noise in either vision or haptics will be examined in section 2.3.

Discussion

Physically interacting individuals tracking the same target can improve their own performance by estimating the partner's movement goal and using it to complement one's own sensory information [45]. The present study extends this observation to demonstrate that individuals adapt their muscle contraction to maximize task information while concurrently minimizing energy. The CNS inconspicuously adapts muscles activation to best combine visual information with the haptic information from the partner's movement. The results from this study as well as from Section 2.1 revealed the surprising ability to adapt the body's viscoelasticity to extracting maximal information during interaction with a partner or with a dynamic environment while concurrently minimizing effort.

2.3 Computational modeling

This section develops an algorithm to understand the adaptation mechanism of humans interacting with various environments (section 2.1) and with other humans (section 2.2). The respective modeling and simulation results

are described in sections 2.3 and 2.3 while the related algorithms and their implementation are detailed in section 2.3. The computational mechanism of adaptation to various environments and human partners yields a predictive coding algorithm to adapt the body viscoelasticity and improve the visual and haptic sensing.

Modeling the adaptive interaction mechanism with various environments

The improvements in the tracking performance observed during interaction with visual and haptic environments described in section 2.1 could be purely due to the mechanical effect of the guidance. To test this possibility, we simulated a computational model according to which cocontraction is modulated to minimize the tracking error, which explains its adaptation when interacting with various dynamic environments [48]. In this model, the cocontraction increases with the tracking error e and decreases with each new trial according to

$$u_{new} \equiv \alpha\, e + (1-\gamma)\, u\,, \quad \alpha, \gamma > 0\,. \tag{2.14}$$

Simulation of the visual noise experiment with this *tracking error minimization* (TEM) model predicted an increase in cocontraction with the visual noise, corresponding to the trend observed in the experimental data, albeit not capturing its variability (Fig.7A). We then simulated its predictions for the guidance bias experiment. The model predicted an increase in the cocontraction with the bias, opposite to what was observed in the experiment (Fig.7B). While the TEM model could capture the change in the cocontraction as a function of visual noise, it cannot explain the results of the guidance bias experiment.

Alternatively, the CNS may be actively modifying the body's stiffness to regulate its haptic sensitivity and use this information to improve motor performance. Since the cocontraction adapted to both visual noise and the guidance bias, it may be determined by the statistical information from vision and haptics, characterized by their respective standard deviations σ_h and σ_v. Specifically, cocontraction could be adapted to minimize the Bayesian prediction error

$$E(u) \equiv \frac{\sigma_h^2(u)\ \sigma_v^2}{\sigma_h^2(u) + \sigma_v^2} \tag{2.15}$$

that depends on the cocontraction through $\sigma_h(u)$. Simulations with this *Bayesian error minimization* (BEM) model predict an increase in the cocon-

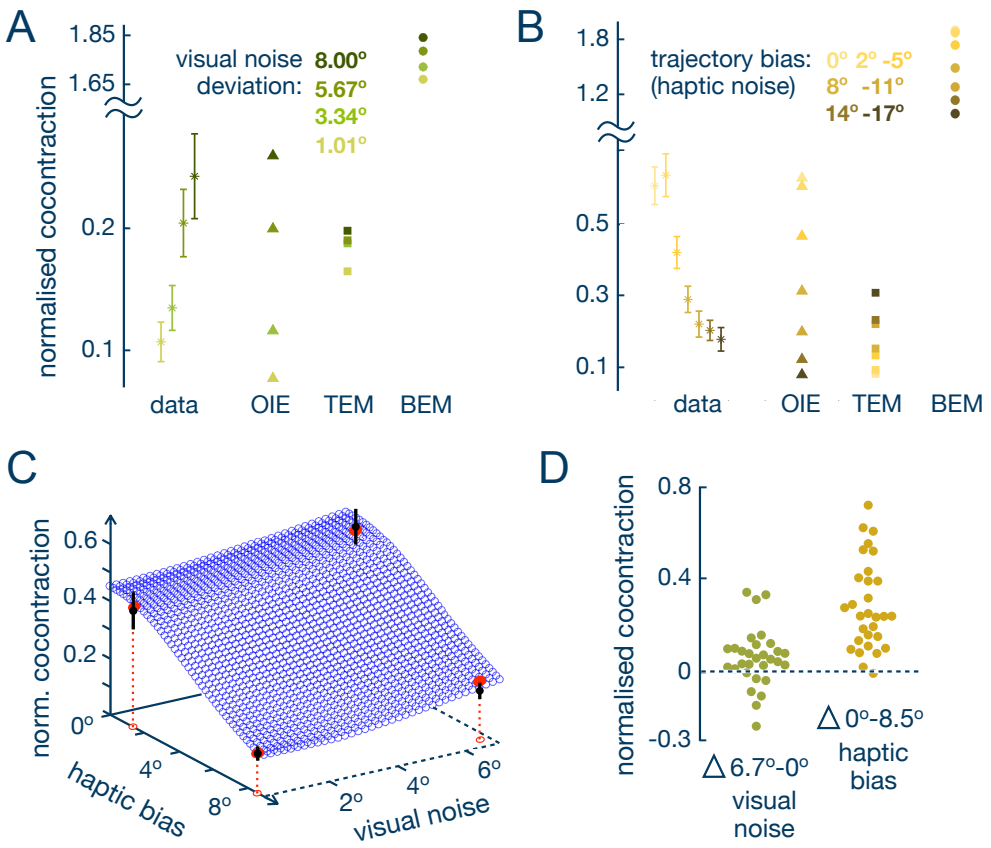

Figure 7: Computational modeling of adaptation to visual and haptic perturbations. (A) The cocontraction in the last block of the visual noise experiment is compared with the prediction of the *tracking error minimization* (TEM), *Bayesian error minimization* (BEM) and *optimal information and effort* (OIE) models. (B) Cocontraction in the last block of the guidance bias experiment with the predictions from these models. TEM showed the opposite trend to the data, the BEM exhibited a correct trend but with diverging values, while the results predicted by OIE resembled the data. (C) The OIE model predicts an increase in cocontraction both as a function of the visual noise and the bias. A third experiment with concurrent changes in visual noise and guidance bias was carried out. The protocol involved 8 blocks of 4 trials with bias and visual noise conditions corresponding to the red dots presented in random order. The corresponding mean values and standard error are shown in black. (D) Corresponding difference of cocontraction with a larger visual noise standard deviation and smaller haptic guidance bias.

traction with greater visual noise (Fig.7A) as well as smaller cocontraction with larger bias (Fig.7B), corresponding to the tendencies observed in the experimental data. However, the cocontraction in the BEM model increases

to values outside of the range observed in the experiments.

These results suggest that while the prediction error is considered by the CNS, the BEM model misses a fundamental mechanism to regulate the overall cocontraction level. Considering the natural tendency to minimize cocontraction during learning [47, 48], we propose that the function consisting of the prediction error and the metabolic cost

$$V(u) \equiv E(u) + \frac{\gamma}{2}u^2\,, \quad \gamma > 0 \tag{2.16}$$

is minimized. Simulations with this *optimal information and effort* (OIE) model exhibit an increase in the cocontraction with greater visual noise (Fig.7A), as well as a decrease in the cocontraction with increasing bias (Fig.7B), leading to values close to the experimental data in both cases.

The OIE model further predicts how cocontraction will be modulated in the presence of both visual noise and guidance bias, illustrated as the blue surface of Fig.7C. A third experiment was carried out to test the efficacy of the OIE model in explaining concurrent changes to visual noise and guidance bias. An aligned ranks transformation ANOVA (ART ANOVA) with repeated measurements revealed that the normalized cocontraction was significantly influenced by the guidance bias ($p<0.001$, $F(1,98)=61.91$), weakly influenced by the visual noise level ($p=0.14$, $F(1,98)=2.16$), and not affected by the training ($p=0.56$, $F(1,98)=0.35$) (Fig. 7D and Figure 3). Post-hoc comparisons revealed how the normalized cocontraction increased with larger visual noise ($p=0.025$) and decreased with a larger haptic bias ($p<0.001$). The cocontraction in this visuo-haptic experiment was indeed modulated by both visual noise and bias as predicted by the OIE model (Fig. 7C).

Recent models [50, 51] clarified how major characteristics of motor memory correspond to the minimisation of motor error and its history. These models however do not possess a mechanism to deal with muscle stiffness so cannot explain above results nor the results from [32]. On the other hand, a range of experimental evidence from arm movements carried out in various spatial, temporal and dynamic conditions suggest that planned actions minimise task error and metabolic cost in the presence of motor noise [48, 52, 53, 54]. However, these studies did not consider sensory noise and its influence on the cost function. Our study provides evidence that the CNS also considers noise in the sensory signals and voluntarily controls the muscle activation to minimise task error and metabolic cost. The CNS adapts the motor commands to improve visuo-haptic perception through an optimal tradeoff of information and energy.

Modeling cocontraction adaptation during interactive performance

To understand the principle behind the cocontraction adaptation observed during human-human interaction in section 2.2, we first tested the computational model of [48] that explains the motor learning taking place in arbitrary novel force fields. Simulation of the learning during the ten trials of each condition with the TEM model of eq.(2.14) predicted cocontraction at a level increasing with the corresponding tracking error (Fig.8A). These predicted results are qualitatively different from the data, such as larger cocontraction in fuzzy relative to the sharp conditions (e.g. compare the fuzzy-fuzzy and sharp-shapr conditions in Fig.8A). Therefore the TEM model cannot explain the cocontraction learned by the dyads during the interactive tracking experiment.

What adaptation factor is missing in the TEM model? The statistical analysis revealed that own visual noise with deviation σ_o was a major factor of the cocontraction level adaptation. A larger cocontraction level will increase the connection's stiffness to the planed movement, thus improve its guidance.

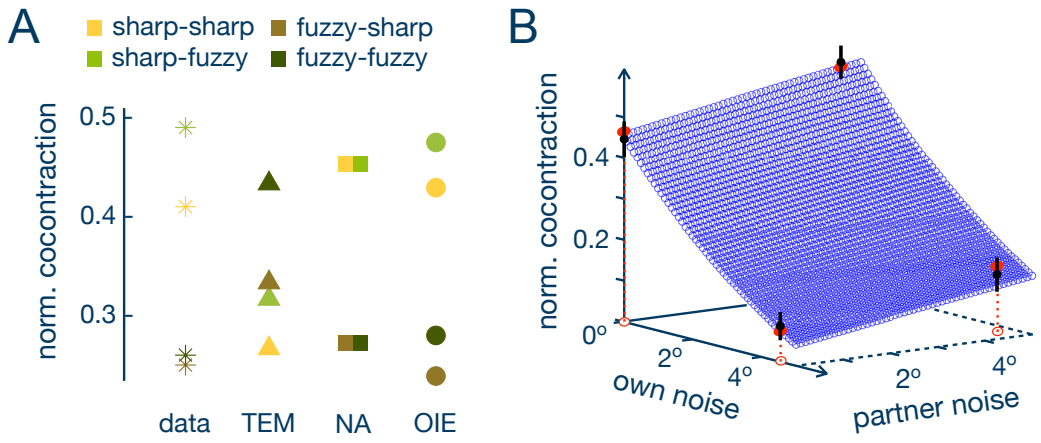

Figure 8: Results of computational modeling the cocontraction adaptation to own and partner noise. (A) Comparison of cocontraction predicted by the three models described in the text. The TEM model predicts a different modulation of cocontraction with varying noise conditions as in the data, the NA model only the modulation with own visual noise. (B) The OIE model prediction (red ovales) exhibits a similar decrease of cocontraction with own noise and increase with partner noise as in the data (black disks with standard error bars).

However, if the planned movement is disturbed by visual noise, a stiffer connection will bring larger noise in the hand control, in which case it would be better to relax the arm. Therefore, cocontraction u should tend to increase, and decrease with visual noise deviation $\sigma_o(u)$:

$$u_{new} \equiv \beta - \alpha\,\sigma_o + (1-\gamma)\,u\,, \quad \alpha, \beta, \gamma > 0\,. \tag{2.17}$$

Simulation with this *noise attenuation (NA)* model yields results with a trend similar to the data, with cocontraction decreasing in the FS and FF conditions (Fig.8A). However the NA model is not able to differentiate between these two conditions, nor between the sharp-sharp and sharp-fuzzy conditions. This suggests that cocontraction adaptation depends not only on own visual noise but also on haptic noise from the partner.

Cocontraction appears to adapt according to the effect it has on the tracking performance. It may depend on the statistical information from own motion plan (guiding my arm movement but affected by own visual noise) or on the partner's interaction (contributing to guide my arm movement and injecting perturbation due to their visual noise). Therefore, we propose that the cocontraction is modulated to maximise information from own visual information and haptic information from the interaction with the partner.

This corresponds to the *optimal information and effort* (OIE) model that could successfully model the interaction with various levels of visual and haptic noise in section 2.3. Here the OIE addresses the tradeoff between haptic guidance and noise attenuation by selecting cocontraction u to minimize the prediction error

$$E(u) \equiv \frac{\sigma_o^2(u)\,\sigma_p^2}{\sigma_o^2(u) + \sigma_p^2} \tag{2.18}$$

and metabolic cost u^2, where $\sigma_o(u)$ results from the effect of own visual noise on the arm movement and σ_p from the interaction with the partner. As can be seen in Fig.8A, the OIE results in less error to the data as the TEM and NA models. More importantly, the OIE model can predict the modulation of cocontraction with both own visual noise and haptic noise from the partner as observed in the data, in contrast to the TEM and NA models (Fig.8B).

Discussion

The experiments of sections 2.1 and 2.2 have shown that CNS inconspicuously adapts muscles activation to best combine visual information with the haptic information from the interaction with the environment or with a partner. The

experimental results and the computational modeling of this section revealed the surprising ability to adapt the body's viscoelasticity, in order to extract maximal information during interaction with a partner or with a dynamic environment while concurrently minimizing effort.

What is the principle of the skilled muscle adaptation mechanism? Above computational modelling suggests that muscle coactivation is adapted to optimise the sensory information from the exchange with the partner and the effort required during the interaction. The picture that emerges from this optimal information and effort (OIE) model is of the CNS adapting muscles' activation to optimise information and energy. This new model extends motor memory models [50, 51] as it includes neuromechanics, thus enabling prediction of interaction forces and muscle activity in interactions. The OIE also extends optimal and nonlinear adaptive control models [55, 52, 53, 48, 54] by considering the sensory exchange during actions.

Previous learning algorithms inspired by the observation of human learning adapt muscles' viscoelasticity to compensate for the interaction with an unknown mechanical environment [48, 56, 57]. While these algorithms are based on the error to the motion plan, the OIE also considers the information that can be gained from the interaction as well as the reliability of these two information sources. An important aspect of the OIE is that it considers how sensor noise will influence motion planning, while traditional stochastic optimal control only considered noise depending on the motor command [53]. This opens up a range of new possibilities to interact with dynamic environments and humans as well as applications for collaborative robots physically interacting with the human operator in surgery or manufacturing [58] and robot assistants for physical training [59]. The OIE is an implementation of predictive coding to adapt the body viscoelasticity in order to minimise the error with multisensory information including haptics, which will be used in PH-CODING.

Algorithms and simulation

Interaction with visual and haptic environments (Results in 2.3)

Haptic noise relative to the target movement is due to the biased reference trajectory relative to the target (resulting in the movement standard deviation σ_b relative to the target trajectory) and to the elasticity of the virtual band [46]. Assuming that these effects are independent and that the band

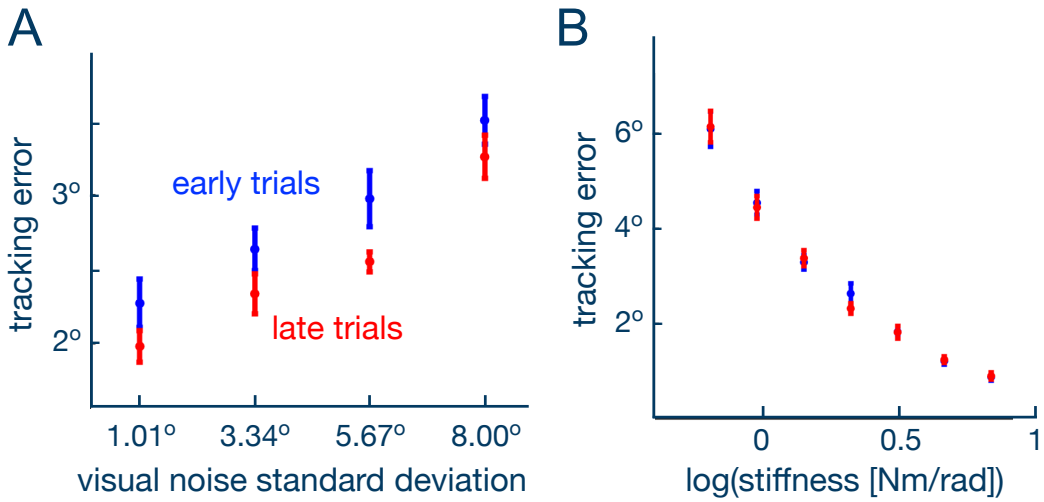

Figure 9: Two control experiments were carried out to isolate the effect of visual feedback and haptic guidance on the tracking performance. (A) In the control experiment with visual noise, the tracking error linearly grew with visual noise, and decreased across all noise levels after learning. (B) In the experiment with haptic feedback only, the tracking error decreased with the log of the elasticity. This relationship did not change with practice.

elasticity results in zero mean noise with deviation $\sigma_\kappa(u)$, the haptic noise deviation can be calculated as

$$\sigma_h^2(u) = \sigma_b^2 + \sigma_\kappa^2(u)\,. \tag{2.19}$$

The effect of the reference trajectory bias is described through

$$\sigma_b = \alpha_b + \delta^\theta \tag{2.20}$$

with subject specific $\alpha_b, \theta > 0$. Two control experiments were carried out to observe the tracking performance as either a function of the visual noise or as a function of the virtual band's elasticity in order to specify the haptic noise.

A *visual control experiment* was carried out to evaluate the influence of the visual noise on the tracking performance. No elastic force was present in this control experiment. Eight right-handed participants not involved in the main experiments (25.01±0.53 years old, including 2 females) participated in this study. The results show that the tracking error is linearly correlated with the visual noise imposed on the target (Fig.9A, [60]). This was modelled as

$$e(\sigma_v) = \alpha_v + \beta_v\,\sigma_v\,, \tag{2.21}$$

where α_v, β_v were identified from a least-squares linear regression with data from late trials.

Next, a *haptic control experiment* was performed to measure how the tracking error depended on the elasticity of the virtual band. In this control experiment, no visual feedback was provided while the wrist was connected to the target reference trajectory with 7 selected levels of elasticity. Another eight participants (7/8 right-handed, 26.75±1.28 years old, including 4 females) participated in this experiment. The experiment was structured in 5 blocks of 7 elasticity $\kappa \in \{0.011, 0.016, 0.025, 0.037, 0.055, 0.081, 0.120\}\,\mathrm{Nm}/^\circ$ presented in random order. In the interaction phase totalling 35 trials, the subjects experienced an elastic force to the target. As expected, the tracking error decreased with increasing elasticity (Fig.9B), which was modelled as an exponential function

$$e(\kappa) = \alpha_h\, e^{-\beta_h \kappa} + \gamma_h\,, \tag{2.22}$$

where α_h, β_h, γ_h were identified from a least-square fit.

To compare the deviations of tracking error due to visual and haptic noise, the error due to haptic noise was transformed to its equivalent value in visual noise. This was carried out by setting $e(\kappa) \equiv e(\sigma_v)$, yielding

$$\begin{aligned} \sigma_\kappa(u) &= \xi_0 + \xi_1\, e^{-\beta_\kappa u}\,, \\ \xi_0 &\equiv (\gamma_h - \alpha_v)/\beta_v\,, \quad \xi_1 \equiv \alpha_h/\beta_v\,, \quad \beta_\kappa \equiv \beta_h/8\,. \end{aligned} \tag{2.23}$$

Tracking error minimization (TEM) For each of the 7 bias levels $\{i\}$, the initial cocontraction level $\{\hat{u}_i(1)\}$ was first set as the initial experimental value $\{u_i(1)\}$. Then, by using the respective trial-by-trial tracking error $\{e_i(k)\}, k = 1, ..., 5$ from the experiment, the adaptation parameters α, γ in the computational model of eq.(2.14) were computed to minimize the error between the learned values after 5 iterations $\{\hat{u}_i(6)\}$ and the corresponding data $\{u_i(6)\}$ in last experiment's trial:

$$(\alpha^*, \gamma^*) \equiv \underset{\alpha,\gamma>0}{\arg\min} \left\{ \sum_{i=1}^{7} \left[\hat{u}_i(6) - u_i(6)\right]^2 \right\}. \tag{2.24}$$

The parameters $\alpha^* \equiv 0.01, \gamma^* \equiv 0.14$ were found by using a grid search with a step 0.01 in the range $[0, 2] \times [0, 2]$.

Optimal information and effort (OIE) A gradient descent optimisation is used to minimize the prediction error and effort in eq.(2.16). Muscle

cocontraction is updated trial after trial using:

$$u_{new} = u - \frac{dV(u)}{du} = -\frac{dE(u)}{du} + (1-\gamma)\,u\,,$$
$$-\frac{dE(u)}{du} = \left[\frac{\sigma_v^2}{\sigma_h^2+\sigma_v^2}\right]^2\left[-\frac{d\sigma_h^2(u)}{du}\right] > 0\,. \tag{2.25}$$

γ and α_b, θ [in the haptic noise model of eqs.(2.19,2.20)] were computed by minimizing the variation of the cost derivative:

$$(\gamma^*, \theta^*, \alpha_b^*) \equiv \underset{\gamma,\theta,\alpha_b>0}{\arg\min}\left\{\sum_{i=1}^{7}\left[\frac{dV}{du}\left[\hat{u}_i(6),\, \sigma_{h,i}(\alpha_b,\theta),\, \sigma_{v,i}\right]\right]^2\right\} \tag{2.26}$$

Assuming $\sigma_v \equiv 2$ for the minimal visual noise standard deviation and using the learned cocontraction data $\{u_i(6)\}$, $\gamma^* = 0.106$, $\theta^* = 2.5$, $\alpha_b^* = 30$ were determined by using a grid search for (θ, α_b) in $[0,3]\times[0,40]$ with steps 0.5 and 1 respectively, where for each gridpoint γ was the solution to

$$0 \equiv \frac{d}{d\gamma}\left[\sum_{i=1}^{7}\left(\frac{dV_i}{du}\right)^2\right]. \tag{2.27}$$

Bayesian error minimization (BEM) BEM was considered as a special case of OIE model with $\gamma \approx 0$. $\theta^* = 3$, $\alpha_b^* = 40$ were determined by using the same grid search as above with $\gamma \equiv 10^{-5}$.

Human-human interaction (Results in section 2.3)

Simulation of tracking error minimization (TEM) For each of the 4 noise conditions $\mathrm{c} \in \{\text{sharp-sharp}, \text{sharp-fuzzy}, \text{fuzzy-sharp}, \text{fuzzy-fuzzy}\}$, the initial cocontraction level $\{\hat{u}_c(1)\}$ was first set as the initial experimental value $\{u_c(1)\}$. Then, by using the respective trial-by-trial tracking error $\{e_c(k)\}, k = 1, ..., 10$ from the experiment, the adaptation parameters α, γ in the computational model of eq.(2.14) were computed to minimize the error between the learned values after 9 iterations $\{\hat{u}_c(10)\}$ and the corresponding data $\{u_c(10)\}$ in last experiment's trial:

$$(\alpha^*, \gamma^*) \equiv \underset{\alpha,\gamma}{\arg\min}\left\{\sum_{\{c\}}\left[\hat{u}_c(10) - u_c(10)\right]^2\right\}. \tag{2.28}$$

The parameters $\alpha^* \equiv 0.5, \gamma^* \equiv 0.06$ were found by using a grid search with a step 0.01 in the range $[0,2]\times[0,1.5]$.

Simulation of noise attenuation model (NA) Using the standard deviation of own visual noise $\sigma_o \in \{0, 4.58^\circ\}$ in each noise conditions, the adaptation parameters α, β, γ in the computational model of eq. (2.17) were identified that minimize the error between the learned values $\{\hat{u}_c(10)\}$ and the last trial's data $\{u_c(10)\}$:

$$(\alpha^*, \beta^*, \gamma^*) \equiv \underset{\alpha,\beta,\gamma}{\arg\min} \left\{ \sum_{\{c\}} \left[\hat{u}_c(10) - u_c(10)\right]^2 \right\}. \tag{2.29}$$

The parameters $\alpha^* \equiv 0.01$, $\beta^* \equiv 0.1$, $\gamma^* \equiv 0.2$, were determined by using a grid search with a step 0.01 in the range $[0, 2] \times [0, 2] \times [0, 1.5]$.

Simulation of optimal information and effort (OIE) A gradient descent optimisation was used to minimize the prediction error and effort in Eq. (2.15). Muscle cocontraction was updated trial after trial using:

$$\begin{aligned} u_{new} &= u - \frac{dV(u)}{du} = -\frac{dE(u)}{du} + (1-\gamma)\, u\,, \\ -\frac{dE(u)}{du} &= \left[\frac{\sigma_p^2}{\sigma_o^2 + \sigma_p^2}\right]^2 \left[-\frac{d\sigma_o^2(u)}{du}\right] > 0\,. \end{aligned} \tag{2.30}$$

The target tracking arises from the mechanical connections to own planned movement and to the partner, while both are subjected to visual noise (Fig. 5C). How to model σ_o? Let σ_{vo} describe the tracking deviation of own wrist movement due to the target cloud. The arm compliance also affects the tracking performance and adds to this noise in the planned movement [46]. Assuming that these two effects are independent and that the arm's viscoelasticity results in zero mean noise with deviation $\sigma_{\kappa o}(u)$, own arm deviation can be calculated as

$$\sigma_o^2(u) = \sigma_{vo}^2 + \sigma_{\kappa o}^2(u)\,. \tag{2.31}$$

The effect of the connection noise was identified in [61] from a control tracking experiment in which participants were guided only from haptic feedback (thus without visual feedback), as

$$\sigma_{\kappa o}(u) = \xi_0 + \xi_1\, e^{-\beta_\kappa u} \quad \xi_0,\, \xi_1,\, \beta_\kappa > 0 \tag{2.32}$$

with $\xi_0 = 5.18$, $\xi_1 = 49.65$, $\beta_\kappa = 6.11$.

In the experiment, the effect of both own visual noise and the partner noise on the wrist movement take two values, resulting in four parameters to identify

for each model: $\{\sigma_{vo}^{(0)}, \sigma_{vo}^{(n)}, \sigma_p^{(0)}, \sigma_p^{(n)}\}$, where (n) corresponds to the cloud target. These parameters, used in the noise models of eqs.(2.15, 2.31, 2.32), were computed by minimizing the variation of the cost derivative:

$$\left(\sigma_{vo}^{(0)*}, \sigma_{vo}^{(n)*}, \sigma_p^{(0)*}, \sigma_p^{(n)*}\right) \equiv \tag{2.33}$$
$$\underset{\sigma_{vo}^{(0)},\sigma_{vo}^{(n)},\sigma_p^{(0)},\sigma_p^{(n)}}{\arg\min} \left\{ \sum_{\{c\}} \left(\tfrac{dV}{du}\left[\hat{u}_c(10),\, \sigma_{o,c},\, \sigma_{p,c}\right]\right)^2 \right\}$$

Using the learned co-contraction data $\{u_c(10)\}$, a grid search for $(\sigma_{vo}^{(0)}, \sigma_{vo}^{(n)}, \sigma_p^{(0)}, \sigma_p^{(n)})$ in $[0, 10] \times [0, 20] \times [0, 10] \times [0, 10]$ with step 0.2 yields $\sigma_{vo}^{(0)*} = 10$, $\sigma_{vo}^{(n)*} = 18.8$, $\sigma_p^{(0)*} = 5.2$, $\sigma_p^{(n)*} = 6$, where for each gridpoint $\gamma^* = 0.65$ was the solution of

$$0 \equiv \frac{d}{d\gamma}\left[\sum_{\{c\}}\left(\frac{dV_c}{du}\right)^2\right]. \tag{2.34}$$

Chapter 3

Robotic haptic exploration

3.1 Predictive coding framework for haptic exploration

In PH-CODING, we want to develop a predictive coding framework for haptic interaction in robots, that can integrate the information from multiple tactile and proprioceptive sensors and explore the environment while extracting essential haptics features and maintaining stability.

To develop a suitable robotic algorithm, let us examine human haptic exploration strategies. Generally, humans use haptic information from the environments to adjust their movement and identify what objects they are dealing with. For example, if I want to find a light switch in a dark room, I will use my hand to gather information by scanning the wall's surface. My CNS will then use the acquired information to understand what I am touching and check how it corresponds to the sensory information I expect from my planned action. During such haptic exploration, I may adapt my motion or finger's impedance to avoid injuries or dangers. With sufficient information I will interpret what I have touched and locate where the light switch is. Inspired by this interpretation, we propose to develop an algorithm composed of two main functions, perception and planning, as is illustrated in Figure 1.

In Figure 1, a robot equipped with multiple tactile and proprioceptive sensors is used to perform haptic exploration in unknown environments. Haptic exploration starts by interacting with an object to gather initial sensory information which is used to yield the prior belief of the object class. The

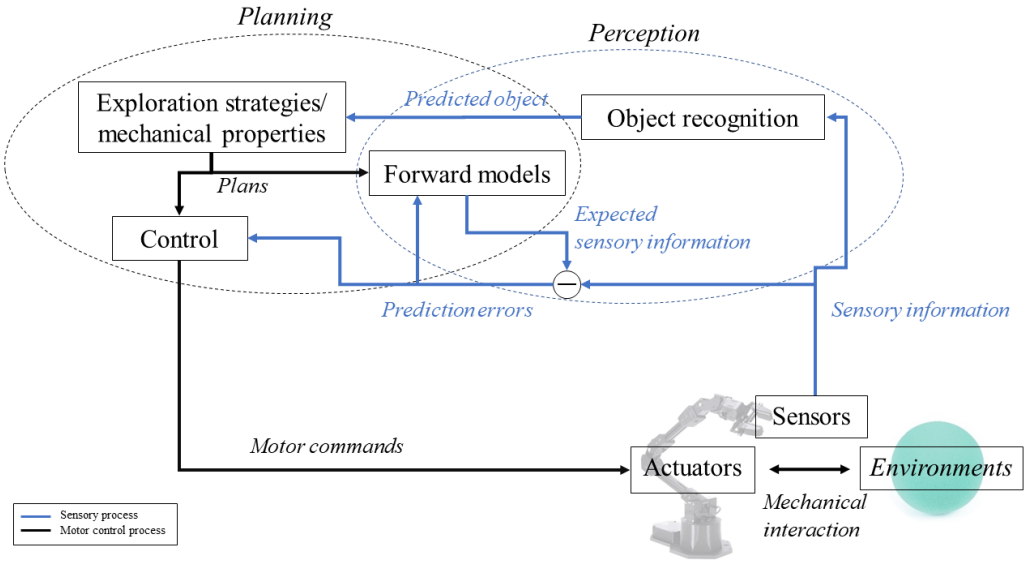

Figure 1: Diagram of haptic exploration in predictive coding framework. The tactile and proprioceptive informations obtained during exploration are used to predict what object the robot is interacting with based on prior knowledge stored in a database. The robot then uses this information to plan motor commands in order to interact effectively with the object. Further information about this object can be obtained by comparing actual with expected sensory information generated from forward models. The prediction error then drives adaptation of the robot control to improve haptic sensing and update forward models, so that the robot can identify the interacted objects more accurately.

motion planning algorithm then selects an appropriate interaction from a set of actions that maximizes the information gain. For example, if the system observes that high speed tapping is useful to distinguish hard objects compared to other actions such as sliding or pressing, this action will be selected. In general, an action with higher mutual information is thus used to interact with the identified object in each iteration until the posterior belief of the object class is sufficiently confident, which provides higher perception accuracy.

Mechanical properties (e.g. stiffness, and viscosity) is important information to collect and identify an object. Suitable interactions with the object need to be designed for the robot to extract these mechanical properties. Some on-line estimation techniques based on the minimization of prediction error are applied to identify them. The planned motion and properties are passed to: *i*) a forward model to update the expectation of sensory information, and *ii*)

to the robot's controller to generate motor commands enabling the actuators to produce meaningful interaction with the environments. Prediction errors are formed by comparing the expected sensory information with measured sensory information. These errors are used to update the forward model and adjust the robot's control to reduce the difference between experience and expectation. Moreover, an adaptive control algorithm will be designed to maintain the robot's stability during the interaction.

These adaptations of the robot will continue until the prediction errors are minimised. As a result, suitable sensory information would provide more accurate identification of the objects. On the other hand, if the prediction errors cannot be minimised, the whole process will (re)identify an object using the previously obtained sensory information and update the database with identified object features. According to this framework, the robot will spontaneously explore, sense, adapt and, finally, identify what it is interacting.

The predictive coding haptic exploration framework is composed of:

- A *sensory system* that recognises objects using sensory information and actively adjusts the sensing parameters to improve perception (as was developed in Chapter 2).
- A *motion planner* that designs exploration strategies including scheduling, motion and parameters optimisation, corresponding to the expected object.
- An *adaptive controller* integrating a forward model, that maintains the interaction stability, controls the force, impedance and trajectory while improving performance.
- An *objects' memory* which is a database of objects' properties collected during previous interactions and constantly updated with experience.

Each of these components will be presented in the next sections. The framework is implemented on an experimental testbed that shown in Fig. 2, consisting of HRG-Hman that is a desktop planar H-shaped robot, a robotic finger equipped with a force sensor (model F/T:Nano17-E, ATI Industrial Automation) and an accelerometer (model ADXL335, Analog Devices). The objects to be recognised are attached on the surface of a wooden frame. This robotic system has been described in the report to deliverable D4.1. Initial tests carried out with this testbed are described in next sections.

The rest of the chapter is organized as follows. In Section 3.2, the object recognition algorithm used for the sensory system will be introduced. The exploration action selection algorithm used for the motion planning are presented in Section 3.3. The adaptive controller described in Section 3.4 integrates a forward model to estimate the object impedance, maintain the interaction stability and ensures quality performance during movement. Based on the obtained results above, the algorithm of object confirmation and database update is described in Section 3.5.

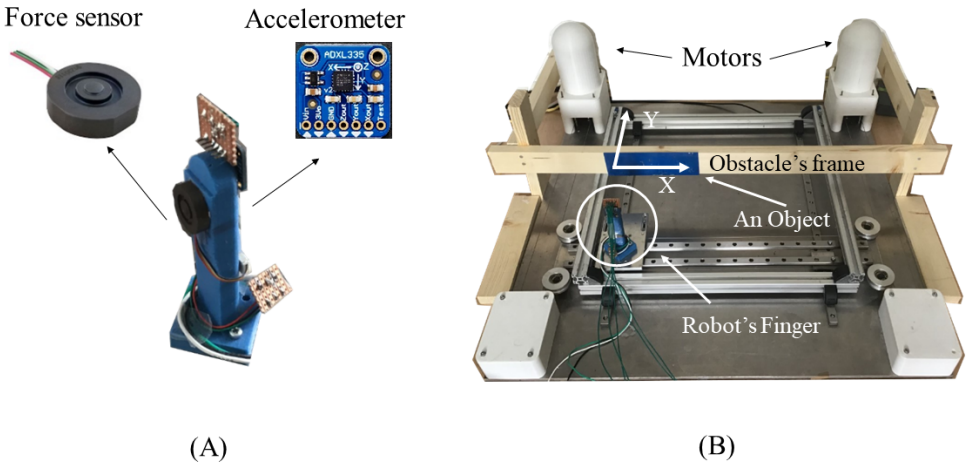

Figure 2: Experimental testbed. (A) A 3D printed robot's finger. The force sensor is attached on the front of finger, while the accelerometer is attached on the back of the finger. (B) H-man with its finger and an obstacle. A wooden frame is used to attach the object (blue area) for the robot to explore. The finger is driven by two motors located on the top right and top left corner of the robot. The finger moves in 2D planar (x and y axis) while the force sensor is facing toward the object's surface.

3.2 Sensory system
Object recognition with initial contact

The sensory system uses tactile and proprioceptive information to quickly and roughly infer the objects with which the robot will interact. The robot can interact with the objects using interaction actions such as tapping, press-

ing and sliding along them. The robot will use different parameters for each of these actions. For example, it can tap a piece of wood at varied speed or scan a piece of sandpaper with different contact forces. The haptic signals such as interaction force, vibrations, pressure and proprioceptive information from the robot will be used to: 1) investigate the characteristics of sensory information for objects obtained with different action conditions, 2) compare methods to extract object's features from the obtained sensory information, 3) apply classification methods to identify objects. Through the initial interaction, the robot will obtain prior belief, i.e. basic information about the objects to be identified.

The robot (equipped with a one-axis force sensor and a three-axis accelerometer on its finger) was programmed to tap the finger on the object with speed 0.02, 0.04, 0.08 m/s on six objects with different mechanical properties: {foam, one-layer sponge, two-layer sponge, plastic, wood, steel}. Figures 3 and 4 show the resulting interaction force and vibration magnitude. The analysis of the sensory information suggests that we can use the peak of an interaction force and a vibration magnitude to separate hard from soft objects. Furthermore, as expected the peak of interaction force and vibration magnitude increased with the tapping speed, also making tactile information for each object more distinguishable. Therefore we may able to identify objects in each group using this tactile information that depends on tapping speeds. A method using this tactile information to classify the six objects was thus developed and investigated.

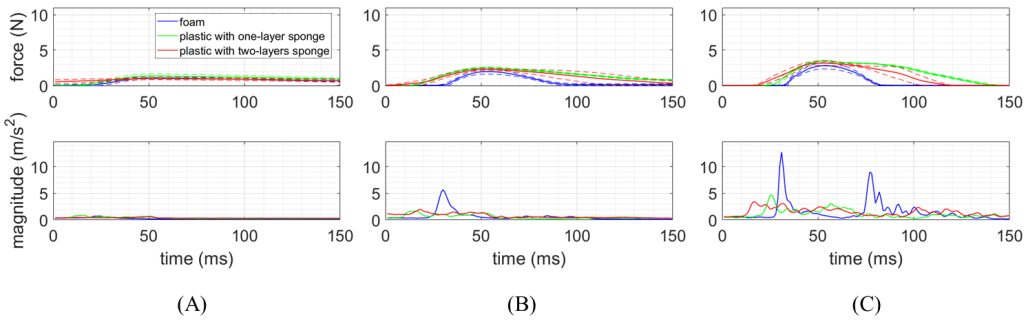

Figure 3: Interaction force and vibration magnitude resulted from tapping of three soft objects. (A) At tapping speed 0.02 m/s, the interaction force and vibration magnitude are are barely distinct. (B) At 0.04 m/s, the interaction force obtained from a steel caps lower than the others while a vibration peak can be observed. (C) Similar interaction force patterns are observed at 0.08 m/s, with two different peaks of vibration magnitude for each object.

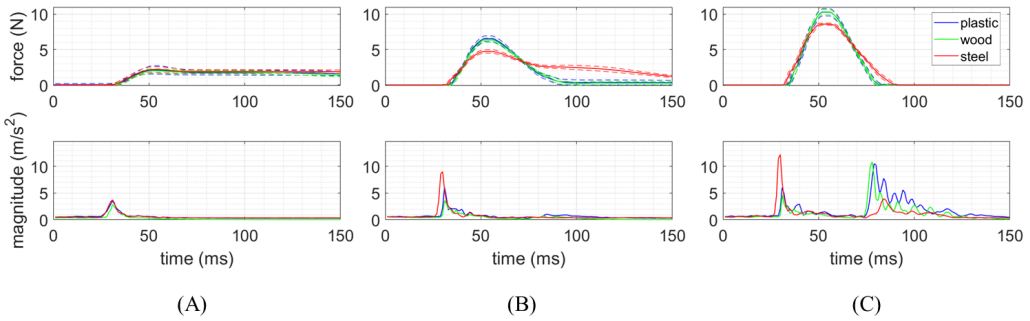

Figure 4: Interaction force and vibration magnitude from tapping on three hard objects. (A) At tapping speed 0.02 m/s, the interaction force and vibration magnitude are barely different in the three objects. (B) At 0.04 m/s, the peaks of interaction force and vibrations are similar for plastic and wood but different for steel. (C) At 0.08 m/s, the interaction force shows similar patterns as at 0.04 m/s, while the ftwo peaks of vibration magnitude is different in the three objects.

Using the Naive Bayes probabilistic classifier, we investigated first the classification of six objects based on the maximum interaction force, maximum vibration magnitude at all tapping speeds. The resulting confusion matrix (Figure 5) exhibits poor classification with 66.27% accuracy rate in average. Second, we separated the tactile information based on the tapping speeds. Figure 6 shows that the classifier still misclassified objects and had 52.9% accuracy rate when it was trained using tactile information at tapping speed 0.02 m/s. However the classification improved at tapping speed 0.04 m/s and

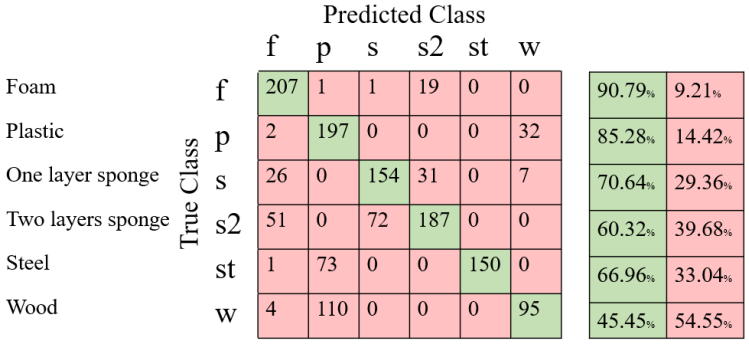

Figure 5: Confusion matrix showing classification results for {f: foam, p: plastic, s: one-layer sponge, s2: two-layer sponge, st: steel, w: wood}. The classifier was trained and tested using data from all tapping speeds. There is confusion for some objects such as between wood and plastic, or between two-layers sponge, one-layer sponge and foam.

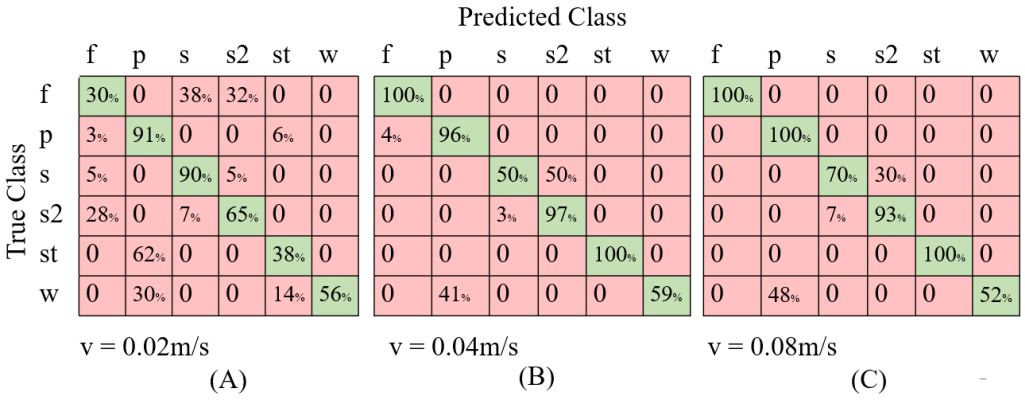

Figure 6: Confusion matrix for {f: foam, p: plastic, s: one-layer sponge, s2: two-layer sponge, st: steel, w: wood} when the classifier was trained and tested with data from tapping at different speeds. (A) At 0.02 m/s, most objects are misclassified except plastics and one-layer sponge. (B) Classification results are better at 0.08 m/s but for some confusion between one-layer and two-layers sponge as well as between wood and plastic. (C) At 0.08 m/s the classification is good but for some confusion between one-layer and two-layers sponge and between wood and plastic.

0.08 m/s, exhibiting an accuracy rate of 82.73% and 81.79% respectively. Increasing speed from 0.04 to 0.08 m/s did not show much improvement with still confusion between plastic and wood.

These results show that the developed classifier can identify six objects based on simple haptic patterns with accuracy rate of 85.83% when the classifier was trained and tested with data at 0.08 m/s tapping speed. However, using only two time domain features confuses between wood and plastic. To attempt tackle this issue the vibration data was analysed using additional factors from frequency domain techniques: continuous wavelet transformation (CWT), discrete wavelet transformation (DWT), and Fast Fourier transformation (FFT).

- First, a CWT with symlet 10 as a mother wavelet was used to transform z-axis vibration in time domain into wavelet coefficients. Figure 7 shows contour plots of the transformed wavelet coefficients at tapping speed 0.04 m/s for the six different objects. It appears that the wavelet coefficients exhibit different patterns in a range of approximately 50-100 Hz. This result suggests using these values of wavelet coefficients as a new feature for the classifier.

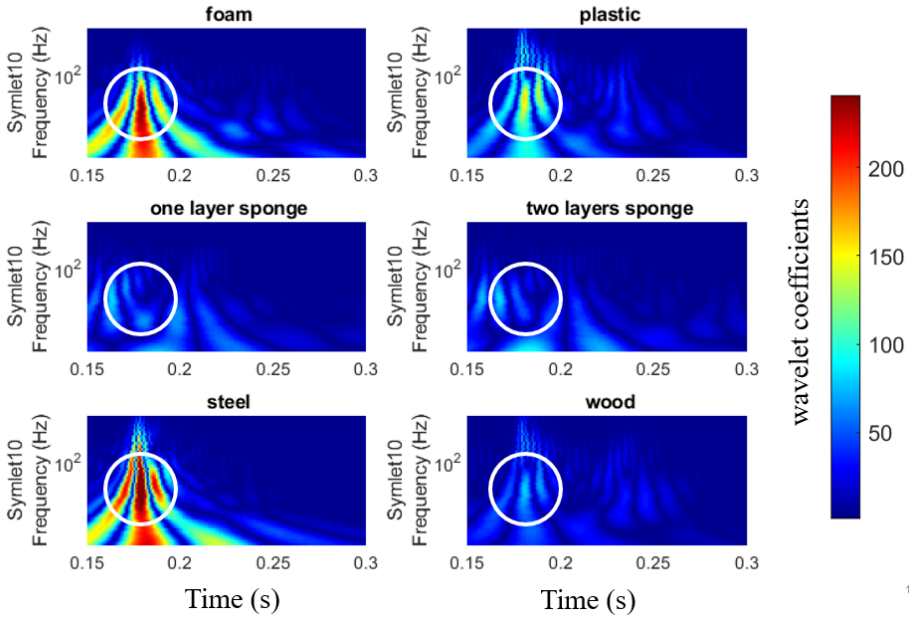

Figure 7: Example of contour plots showing wavelet coefficients obtained using CWT to transform vibration data at tapping speed 0.04 m/s into time-frequency domain. Each object exhibits individual patterns in particular for frequencies in the range 50-100 Hz (white circle).

- Second, a CWT with symlet 10 as a mother wavelet was used to transform z-axis vibration in time domain into wavelet coefficients in frequency domain. In this case, the root mean square of wavelet coefficients for each frequency range was calculated and used as features for the classifier.
- Third, a four-level DWT with symlet 10 as a mother wavelet was used to decompose z-axis vibration in time domain into four levels of wavelet composition. The peak of amplitude for each level of wavelet composition was used as features for the classifier.
- Fourth, a FFT technique was used to transform a z-axis vibration from time into frequency domain. In this case, we divided the frequencies into 6 ranges: {0-50, 50-100, 100-150, 150-250, 250-350, 350-500} Hz. The peak of vibration amplitude for each of these frequency ranges was used as a feature for the classifier.

Figure 8 shows the accuracy rate for all cases using features extracted from time domain combined with above frequency domain features. Figure 8 (A)

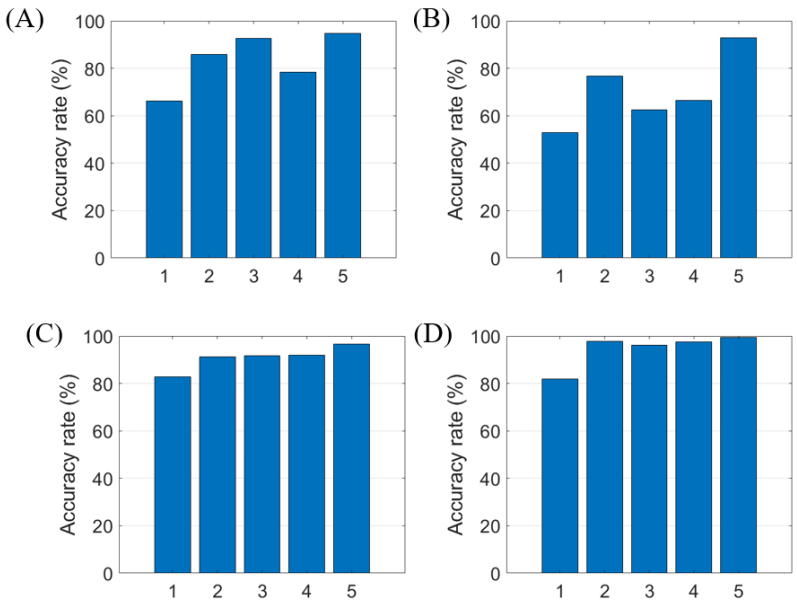

Figure 8: Comparison of accuracy rate with the developed classifier using different sets of features (A) at all tapping speeds, (B) at 0.02 m/s, (C) at 0.04 m/s, (D) at 0.08 m/s. X-axis labels describe the classification factors used: {1: peak interaction force and vibration, 2: as in 1 and peak wavelet coefficients of vibration in 50-100 Hz (CWT), 3: adding to 1 the rms wavelet coefficients of vibration in all frequency ranges (CWT), 4: adding to 1 the peak of vibration amplitude found in four-level of wavelet composition (DWT), 5: adding to 1 the peak vibration amplitude for 6 ranges of frequency (FFT)}.

shows the accuracy rate when the classifier was trained using features from all tapping speeds. The results showed that classifier using peak values of interaction force, vibration magnitude, and vibration amplitude extracted using FFT provided the highest accuracy rate at 94.82%. Figures 8B,C,D, show the accuracy rate with data from tapping speeds at 0.02, 0.04 and 0.08 m/s, respectively. The accuracy rate still increased with the tapping speed but for the FFT classifier that provides high accuracy rate with values over 90% in all cases.

Overall, these results show that adding frequency domain features improves the object classification. A high accuracy rate can be achieved by using features with peak values of interaction force, vibration magnitude, and the frequency spectrum extracted using FFT. Increasing the speed of tapping can improve the accuracy rate although too large impact may damage the material. These results suggest that tactile information obtained from the

initial contact (tapping with high speed) can be used to quickly infer the object a robot is interacting with. However, the prediction accuracy is not sufficient when interacting with objects of similar stiffness, such as wood and steel. Other interaction actions such as sliding may be more appropriate to distinguish them. In the next section, we expand the action set by considering sliding and pressing and develop a motion planning algorithm to select the optimal action for a specific object.

3.3 Motion planner *to select the optimal exploration action*

The motion planner determines the optimal interaction to improve the perception accuracy and plan robot's movements based on the detected object to manipulate. As an example, the database of sensory information in three actions {tapping, sliding, pressing} with different conditions would be acquired and used to determine the optimal actions. According to predictive coding principles, we used conditional mutual information to measure how much uncertainty is reduced in predicting object class X, if observation O is made by an action A, where X, O, A are random variables. The *conditional mutual information* is defined as

$$I(X; O|A) = H(X|A) - H(X|O, A) \tag{3.1}$$

where $H(X|A)$ is the entropy of predicting object class X with knowledge from action A, and $H(X|O, A)$ is the entropy of predicting object class X with knowledge of observation O and action A. The optimal action will reduce uncertainty of prediction thus correspond to the highest value conditional mutual information:

$$A^* = \arg\max_A I(X; O|A) \tag{3.2}$$

If we assume that object class X and action A are independent, and as our object class X is a discrete variable since we are in a classification problem, the conditional mutual information can be rewritten as:

$$I(X; O|a) = H(X) - H(X|O, a) = \sum_x \int_O P(x)\, P(o|x, a)\, \log \frac{P(o|x, a)}{P(o|a)}\, do \tag{3.3}$$

where $x \in X$, $o \in O$, and $a \in A$. $P(o|x, a)$ is a probability of observation o given that object class x and action a can be estimated the same as $P(o|a)$

which is probability of observation o given that action a during training phase of the classifier. In the discrete variable case, those two probabilities can be estimated from a look-up table of parameters stored by experience. $P(x)$ is a prior belief of being object class x which could be obtained from the Naive Bayes classifier in section 3.2.

The Naive Bayes classifier calculates the posterior probability of object class x given that observation O and action a using Bayes's Theorem:

$$P(x|O,a) = \frac{P(O|x,a)P(x)}{P(O|a)} \tag{3.4}$$

where $P(O|x,a)$ is a likelihood of observation O given that object class x and action a, $P(x)$ is a prior belief of being object class x, and $P(O|a)$ the prior belief of observation O given action a. This posterior can be used as a prior belief for next iteration $i+1$, i.e. $P(x)_{i+1} = P(x|O,a)_i$, allowing us to use the prediction from previous iteration to select the action in order to gain more useful information.

Validation of action selection algorithm

The overall structure of action selection algorithm is shown in Figure 9. The algorithm starts with the initial guess of prior for all objects which, e.g. the belief obtained form the initial contact or 1/(number of objects) if there is no such knowledge. This prior is used to find the conditional mutual information using eq.(3.3). The optimal action is then selected based on the calculated conditional mutual information using eq.(3.2). This selected action is used by the robot to interact with the object and retrieve the observation. This observation is then fed to the classifier in order to calculate the posterior using eq.(3.4). If the values of posterior for at least one object class is higher than 0.95 or there are already more than five iterations, the highest posterior of object class x is selected and the classifier concludes that the object belong in object class x:

$$X^* = \arg\max_x P(X;O|A^*) \tag{3.5}$$

otherwise the current posterior will be used as the prior for next iteration.

To illustrate how the algorithm works, the robot of Figure 2 was used to interact with ten different objects: {hard silicon, soft silicon, solid box of paper, wobbling box of paper, styrofoam, sponge, sponge with polyethylene foam surface, wood, wood with polyethylene foam surface, steel}. The robot was programmed to use three actions: {pressing, sliding, tapping} in order

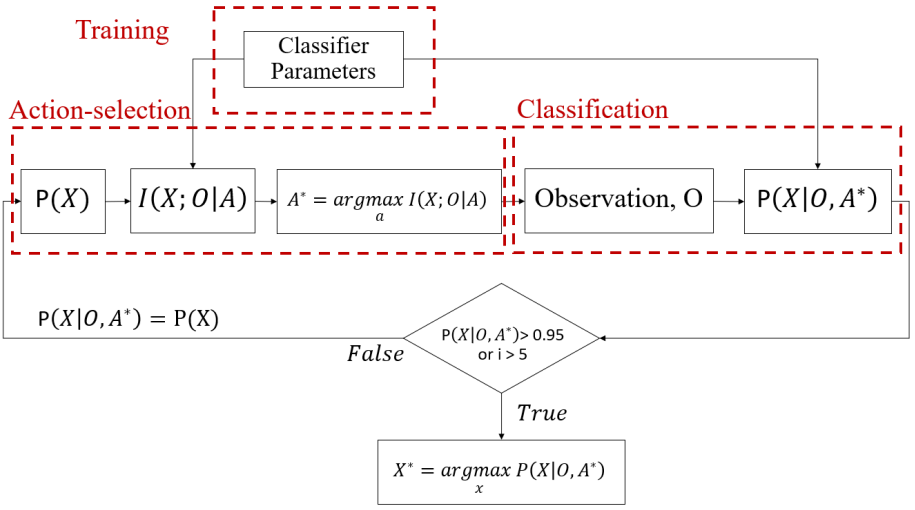

Figure 9: Structure of the action selection algorithm. There are three main parts shown in red. First, training uses a database to train the Naive Bayes classifier and acquire parameters. Second, to select an action, it uses the parameters and prior belief from the previous iteration to determine the action with the maximal value of conditional mutual information. Third, together with parameters acquired during training, observations from the interaction with the object are used to calculate posteriors thereby inferring which object the robot interacts with. The algorithm will continue until the posterior belief about an object reaches 0.95 or after five iterations. The object class yielding highest posterior will be selected as the predicted object.

to form a database of tactile information in the form of interaction force and vibration. More precisely, the average normal force was used as observation for action pressing, a standard deviation of vibration values during sliding as the observation for this action, and the maximum values of normal force for action tapping. This data was used to train the developed classifier as well as to test the action selection algorithm. For simplicity, the action-selection algorithm simulation is performed off-line based on the collected data.

Figure 10 shows the confusion matrix obtained after simulating the testing of 10 objects presented randomly for 3000 trials with above action selection algorithm. The classifier can distinguish all objects but confuses wood and steel. The average detection rate was 84.83%.

Figure 11 shows how the prior belief changes after each iteration when the robot adapts its action to gain most information during interaction with the objects. The true object is class four which is a hard silicon. The prior belief

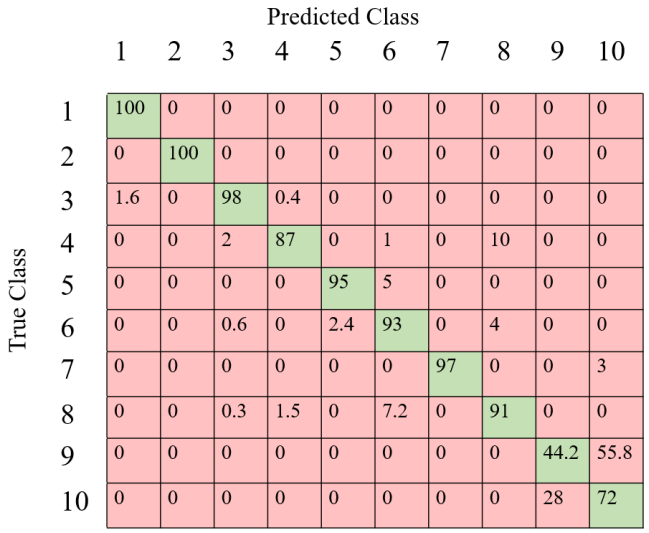

Figure 10: The confusion matrix showing accuracy rate of classification in percentage when classifier using action-selection algorithm. The numbers 1-10 on axis presents objects class as a soft silicon, a sponge, a sponge with polyethylene foam surface, a hard silicon, a wobbling box of paper, a styrofoam, a solid box of paper, a wood with polyethylene foam surface, a wood, and a steel respectively.

of all objects was initialised at 1/10. Based on this information, the algorithm selected sliding as the first action for the robot to maximally increase tactile information. The tactile information obtained from the sliding was then used to calculate the posterior. Since, the values of posterior ≤ 0.95 the current posterior is used in next iteration to determine the most useful action to gain information. The process is repeated until the posterior > 0.95 as in the bottom graph. The classifier then concluded that it interacted with object number four. We can see that the algorithm adapts the action to gain useful tactile information for the classifier, changing the action from sliding to pressing in the second iteration. This is because it intends to determine whether the object is soft (object classes 1-5) or hard (classes 5-10) by using pressing to check the object's stiffness.

We then compared the performance of our action selection algorithm with a classifier without action selection, the classifier with a fixed action, and the classifier with random actions. In the classifier without action selection algorithm and the classifier with a fixed action, sliding was selected as the action providing highest conditional mutual information with the uniform 1/10 prior. For the random action and action selection algorithms, actions that do not provide necessary tactile information were added in order to

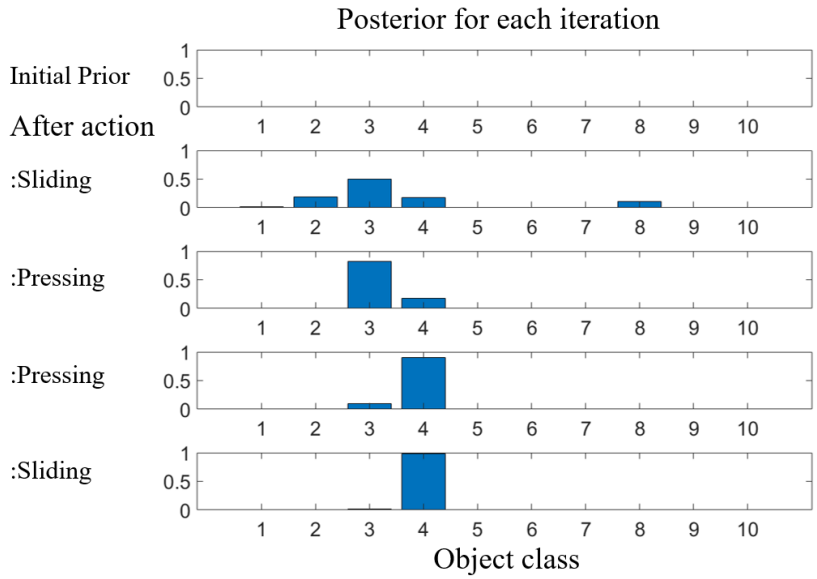

Figure 11: Evolution of prior and actions at each iteration when the robot interacts with the object class 4. The objects are: {soft silicon, sponge, sponge with polyethylene foam surface, hard silicon, wobbling box of paper, styrofoam, solid box of paper, wood with polyethylene foam surface, wood, steel}.

verify that the action selection algorithm is able to choose the right action.

Figure 12 compares the accuracy rate obtained with these algorithms. The results showed the classifier with action selection had the highest accuracy rate (84.83%) while other algorithms had approximately 40-60%. Note that this slightly improves the accuracy rate of 82.73% from the initial tapping with a single feature (maximal interaction force or vibration amplitude) but not as high as the previous results with multi-features after adding the frequency components of vibrations (94.82%). This is because only one sensory information was used in this study. This could cause some confusions between the object classes 9 and 10 as shown in Figure 10. We will therefore expand the algorithm to work with multiple observation features, which should help increasing the prediction accuracy.

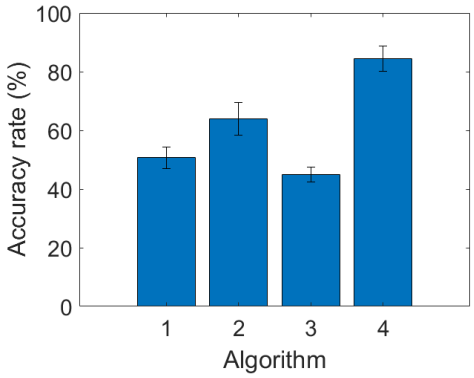

Figure 12: Comparison of accuracy rate among classifiers algorithms: {1: classifier without action selection algorithm, 2: with fixed action, 3: with random action, 4: classifier with action-selection algorithm}. The classifier with action-selection algorithm yields the highest accuracy rate of 84.83%, random action yields the lowest accuracy of 45%.

3.4 Adaptive controller with the estimation of the surface impedance

Mechanical properties like stiffness and viscosity are important features characterising objects to be manipulated with the robot. An adaptive controller is designed to estimate the object's viscoelasticity, which indents the object's surface based on suitable feedforward motor commands (that may be known from a forward model of the robot's dynamics). By measuring the resulting displacement and the interaction force, and using the forward force, the object's impedance around the interaction point can be identified.

The overall structure of the adaptive indentation movement control is shown in Figure 13. Sensory noise in the measurement and process noise in the dynamics of the robot are considered. Dual states and impedance estimators are designed, which are inter-connected. The proprioceptive information (position, velocity) is estimated through Kalman filtering techniques, while the mechanical properties are updated by comparing the sensory prediction and measurement.

The robot is modelled as a pointmass with zero mean normal distributed motor noise with covariance Q i.e. $n_w \sim \mathcal{N}(0, Q)$:

$$m\,\ddot{x} = u + N + n_w. \tag{3.6}$$

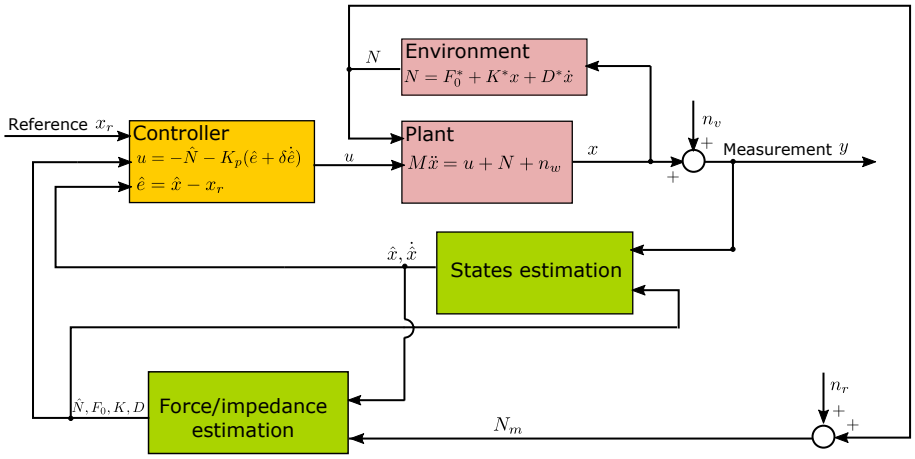

Figure 13: Control diagram of the object's viscoelasticity estimation with dual states and parameters estimation. Sensory noise is considered in measurement of the interaction force and position, as well as process noise in the dynamics of the robot. A recursive estimator is designed to predict interaction force and mechanical properties of the surface, and a Kalman filter is used to estimate the position and velocity of the robot by integrating the model prediction and sensory information.

The position measurement is affected by sensor noise $n_v \sim \mathcal{N}(0,\, R)$:

$$y = x + n_v \,. \tag{3.7}$$

Linearisation of the object's mechanics in interaction with the robot yields

$$N = F_0^* + \kappa^* x + D^* \dot{x} + n_r \,. \tag{3.8}$$

where F_0^* is a feedforward force term due to the object's movement, κ^* its stiffness, and D^* its viscosity. $n_r \sim \mathcal{N}(0,\, G)$ is the sensory noise of interaction force measurement.

The system (3.6) represented in state space and discretised yields

$$\begin{aligned} x_{k+1} &= Ax_k + B(u_k + N_k + n_{w,k}) \\ y_k &= Cx_k + n_{v,k} \end{aligned} \tag{3.9}$$

where $A \equiv \begin{bmatrix} \delta & 1 \\ 0 & 1 \end{bmatrix}$, $B \equiv \begin{bmatrix} 0.5\,\delta^2/m \\ \delta/m \end{bmatrix}$, $C \equiv [1\,0]$ and δ is the time step.

Parameter	Value	Unit
Mass m	2	Kg
Sponge stiffness κ^*	300	N/m
Sponge viscosity D^*	30	Ns/m
Feed-forward force F_0^*	10	N
Proportional gain K_P	500	N/m
Derivative gain ratio ξ	0.04	Ns/m
Process noise covariance Q	$[25\ 0; 0\ 25] \times 10^{-4}$	m
Sensory noise covariance R	4×10^{-4}	m
Initial priori covariance matrix P	[10 0;0 10]	-
Time step δ	0.001	s
Learning rate γ	300	-

Figure 14: Parameter list for the simulation of a mechanical interaction with a sponge.

Position and velocity estimation We use a dual state and parameter estimation scheme, including a state observer and a parameter estimator, which are inherently inter-connected and updated recursively. The position and velocity of the robot are estimated by a standard Kalman filter, and the force and impedance used in the model are identified from model reference adaptive control.

Force and impedance estimation Now that we have the estimated position and velocity, the linear second order system

$$\hat{N} = F_0 + \kappa\hat{x} + D\dot{\hat{x}} \tag{3.10}$$

is used to estimate the force F_0, stiffness κ and damping ratio D with model reference methods in adaptive control. The prediction error of the interaction force

$$J = \frac{1}{2}\left[N - \hat{N}(F_0, \kappa, D)\right]^2. \tag{3.11}$$

is minimised through a gradient descent method:

$$\dot{p} = -\gamma \frac{dJ}{dp}, \quad p = [F_0, \kappa, D]^T, \quad \gamma > 0 \tag{3.12}$$

where γ is the learning rate. The discrete iteration equations for each of the parameters are then

$$\begin{aligned} F_{0,k} &= F_{0,k-1} - \gamma \frac{\partial J}{\partial F_0}\Delta = F_{0,k-1} + \gamma(N_k - \hat{N}_k)\Delta \\ \kappa_k &= \kappa_{k-1} - \gamma \frac{\partial J}{\partial \kappa}\Delta = \kappa_{k-1} + \gamma(N_k - \hat{N}_k)\hat{x}_k\Delta \\ D_k &= D_{k-1} - \gamma \frac{\partial J}{\partial D}\Delta = D_{k-1} + \gamma(N_k - \hat{N}_k)\dot{\hat{x}}_k\Delta \end{aligned} \tag{3.13}$$

There is redundancy in these parameters as the interaction force is the single input, so a persistently exciting signal (PE) is required for the interaction force to guarantee the convergence of the estimation to the physical value.

Simulations

This simulation example will test the functionality of the adaptive controller and illustrate how it can estimate the position from noisy sensory information and identify a sponge's viscoelasticity through indentation. The parameters used for the simulations are listed in Figure 14. A persistent excitation is provided by a sinusoidal movement with reference trajectory $x_r(t) = 0.015\sin(15t)$ m applied on the object's surface. The driving motor

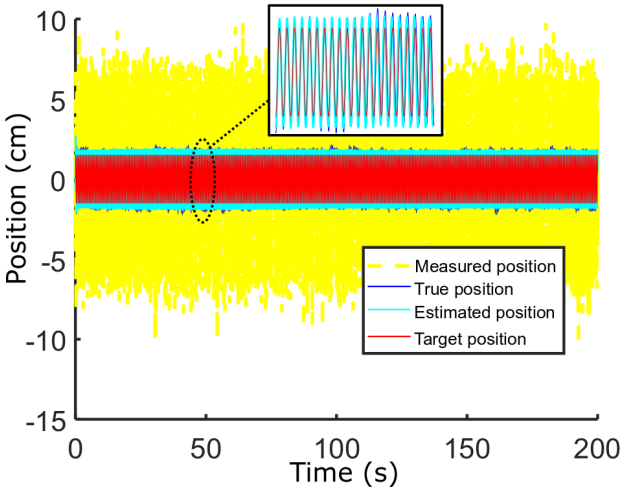

Figure 15: The comparison between the measured position, estimated position, internal true position and the target position. Although there is large noise in the measurement, the designed estimator could predict the position. The controller, based on the estimated states, drives the robot to follow the reference trajectory.

commands are composed of a feedforward term $v_k = -\hat{N}_k$ to compensate the predicted interaction force, where $\hat{N}_k$ is the estimated interaction force, and a feedback term $w_k = -K_P(\hat{e}_k + \xi\dot{\hat{e}}_k)$ to maintain stability, where $\hat{e}_k = \hat{x}_k - x_{r,k}$ is the estimated tracking error, $x_{r,k}$ the planned trajectory, K_P the proportional gain and ξ the derivative gain ratio. The indentation signal is thus $u_k = w_k + v_k$.

The measured and estimated robot positions are shown in Figure 15. It can be seen that the sensory information (yellow dashed lines) contains large noise compared to the true positions (blue lines). Using a Kalman filter, the estimated positions (cyan lines) could follow closely with the true positions. The controller could basically track the fast-varying reference trajectory (red lines), although there are overshoots (around 2 cm) at the turning points. The estimated interaction force and mechanical properties are presented in Figure 16. Fig.16a shows that the estimator could predict the interaction force accurately even before convergence of the stiffness, viscosity and feedforward force terms, as shown in panels b-d. This is due to the redundancy between the interaction force and the mechanical properties, so that the parameters

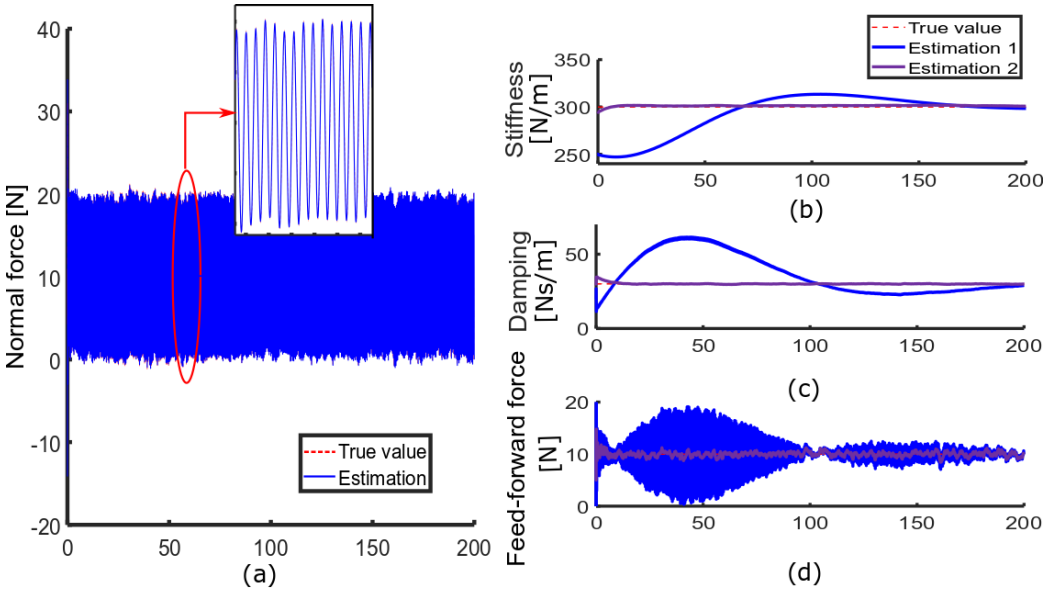

Figure 16: Prediction of interaction force and mechanical properties of a sponge through indentation. Panel a shows that the prediction of the interaction force through the model is consistent with the measurement. Panels b,c,d show the estimation of stiffness, viscosity and feedforward force, respectively. When the object identification is accurate and the initial values for estimation is close to the true values, the estimation converges faster and is more accurate.

converge more slowly to the true values. The blue lines is the estimation with random initial values while the purple lines is the estimation by using the initial guess values from the object recognition. The results reveal that when the object identification is accurate and the initial values for estimation are close to the true values, the estimation process becomes faster and yields more accurate results.

Figure 17 compares the control force and tracking error between the designed controller and the controller with only feedback term. Our controller predicts the interaction force from the forward model and produces a real-time feedforward force that opposing the interaction force. This avoids the sudden perturbation from the unexpected interaction force, and reduces the tracking error. Accordingly, the required control force is largely reduced in the beginning, when there was large tracking error and significant force was needed to drive the robot back to the reference trajectory. As a result, the controller enhances the stability of the robot during exploration, making it more robust to different surface materials. This simple example of indentation movement shows the functionality of the proposed adaptive controller. It will be implemented within the haptic explorative system to validate its effectiveness in

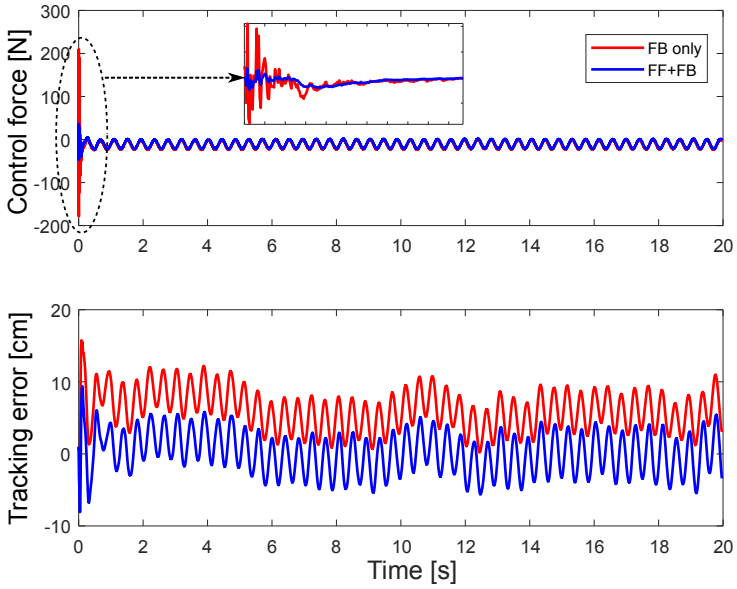

Figure 17: The comparison of the control force and tracking error between designed controller and the controller with only feedback term. It shows that without the feed-forward term to compensate of the interaction force through prediction, there is larger tracking error and the control force is significantly large in the beginning to enable the robot to follow the reference trajectory.

experiments. Furthermore, we will extend it to the haptic exploration with exploratory movements along the object's surface and estimate surface properties such as friction. These surface properties will be used together with the information obtained from the sensory system to confirm the prediction of the object and update the database of objects properties as described in the next section.

3.5 Dynamic objects' memory

The developed sensory system, motion planner and adaptive controller are integrated into a predictive coding algorithm for haptic exploration. The mechanical properties from the adaptive controller can be used to confirm the class of the object that the sensory system and motion planner predict (Figure 18). The structure consists of these parts: an object classifier, a motion planner, an impedance estimator, a motion controller, object confirmation

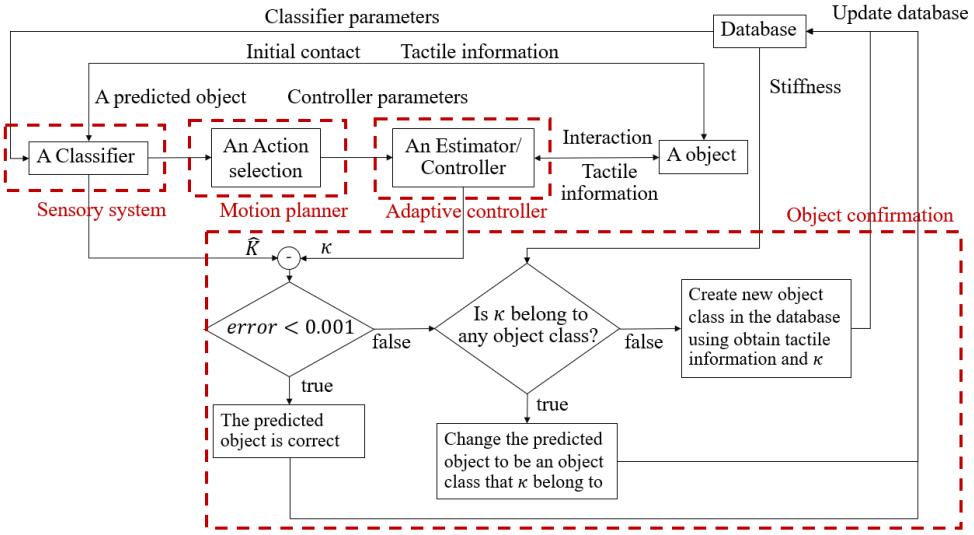

Figure 18: Scheme of robotic haptic exploration algorithm. The classifier uses tactile information from an initial contact to predict an object class, which is used to select a suitable action and controller's viscoelastic parameters. While interacting with an object, the controller can refine these mechanical parameters, which are used to check whether the correct object was selected. If the estimated stiffness differs by more than a threshold (here 0.001), the prediction is replaced with the object that has the most similar stiffness in the database. In case no suitable object is found the new object's parameters are stored in the memory.

and database update.

The algorithm begins with data from a limited set of objects. The classifier described in Section 3.2 will predict an object's rough properties using the tactile information obtained from an initial contact. This predicted object is fed to the motion planner and controller which is described in Sections 3.3 and 3.4 to choose the proper parameters for an object's interaction. In this case, the parameter is the initial guess of object's stiffness values for the controller, which will be refined during interaction. This fine estimation can be used to confirm the predicted object by measuring the estimation error

$$error = \left| \frac{\kappa - \hat{K}}{(\kappa + \hat{K})/2} \right| \tag{3.14}$$

where κ is the estimated stiffness from the controller and $\hat{K}$ the initial guess of stiffness from the classifier. If the difference is not higher than the threshold θ, the predicted object is already correct. If the difference is higher than the threshold θ, the estimated stiffness is used to check in the database whether the corresponding object already exists or not. If the estimated stiffness is not in an acceptable range of stiffness in the database, this new object will be added to the memory.

A simulation was carried out to test the proposed framework, using the same set of objects with as in section 3.3. However, the classifier was only trained using maximum interaction force and vibration obtained when the robot tapped on a soft silicon, a sponge, and a foam at the start. The real stiffness for all objects was assumed to be in the range of 50-1050 N/m as shown in figure 19. The threshold θ was set to be 0.001. The acceptable range of stiffness is 60 N/m. The simulation was done for 1000 trials. In one trial, the algorithm interacts with one random object picked from 10 objects and

Test object	Assumed stiffness (N/m)
Soft silicon	50-150
Sponge	150-250
Sponge with polyethylene foam surface	250-350
Hard silicon	350-450
Wobbling box of paper	450-550
Styrofoam	550-650
Solid box of paper	650-750
Wood with polyethylene foam surface	750-850
Wood	850-950
Steel	950-1050

Figure 19: Table of stiffness range for the ten objects used in the simulation.

classifies the object. Afterwards, the algorithm will collect the information of the object in the database and use it for the next trial.

The evolution of the number of recognised objects in the memory is shown in Figure 20. At the beginning, the database has only first three objects that it have learned in the training phase. After the algorithm finished learning all objects data during the exploration, the memory has information of eleven objects in total in the end. However, the correct number of object class is ten. This incorrect number of the object class in the database might be caused by the value of acceptable range of stiffness. If the value is too low, the algorithm will determine that the estimated stiffness does not belong to any range of stiffness in the database, then it creates a new label for it. If the value is too high, the algorithm will put the estimated stiffness to some object class randomly and can lead to the wrong one. To improve this, the value of acceptable range of stiffness needs to be optimized in further experiments.

The top panel of Figure 21 shows the confusion matrix from the results obtained with the proposed algorithm, which exhibited an average accuracy rate of 77.3%. The misclassified objects seem to have similar stiffness, which may be due that the acceptance range selected in object confirmation may not be able to divide object classes appropriately for the stiffness in between. For example, the wood could be clustered with the steel. The bottom panel of Figure 21 shows the confusion matrix obtained without object confirmation procedure. It exhibits an average accuracy rate of 11.3%, as it only classified the objects based on the initial object classes used for the initial learning.

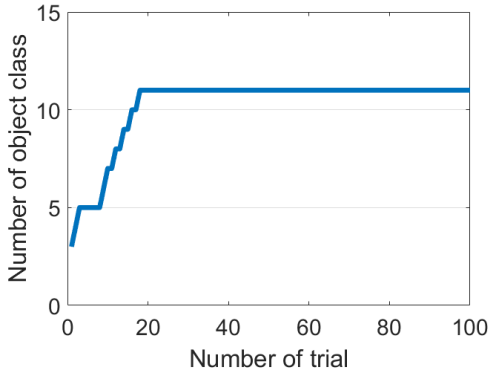

Figure 20: Evolution of memory size. There are initially 3 object classes which are used to train the database. New object classes are added when the algorithm encounters an unknown object. The memory keeps adding new object classes until trial 20, after which it remains at 11 as no unknown object is encountered.

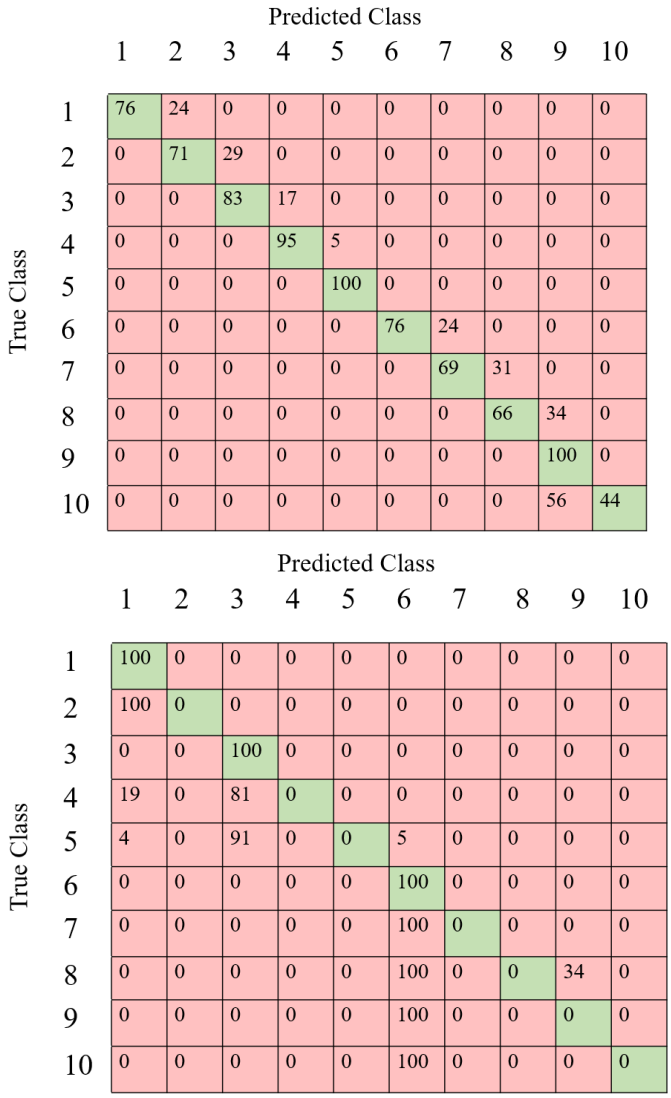

Figure 21: Top penal: confusion matrix obtained with the algorithms of Sections 3.2-3.4 and dynamic memory. Bottom penal: without object confirmation based on the estimated stiffness. Objects are: {soft silicon, sponge, sponge with polyethylene foam surface, hard silicon, wobbling box of paper, styrofoam, solid box of paper, wood with polyethylene foam surface, wood, steel}.

This shows the importance of the objects' memory adaptation process.

In conclusion, the simulation results have shown that the proposed algorithm is able to integrate new objects while it does not grow indefinitely. The dynamic objects' memory enables the classifier to feed useful information, which is initial guess of stiffness value, to the controller for estimating more

accurate parameters. However, some points need to be further developed such as designing a more flexible algorithm for guessing the stiffness value as well as for learning new information from unknown objects, and expand the actions executed by the motion planner.

Bibliography

[1] S. J. Lederman and R. L. Klatzky. Haptic perception : a tutorial. *Attention, Perception, & Psychophysics*, 71(7):1439–1459, 2009.

[2] N. Hogan. Impedance control: An approach to manipulation. In *1984 IEEE American control conference*, pages 304–313, 1984.

[3] A. Prochazka. Proprioceptive Feedback and Movement Regulation. In *Comprehensive Physiology*, chapter 3. John Wiley & Sons, Inc., Hoboken, NJ, USA, 1 2011.

[4] K. J. Friston, Jean Daunizeau, James Kilner, and Stefan J. Kiebel. Action and behavior: a free-energy formulation. *Biological Cybernetics*, 102:227–260, 2010.

[5] K. J. Friston, J. Mattout, and J. Kilner. Action understanding and active inference. *Biological cybernetics*, 104:137–60, 02 2011.

[6] T. J. Prescott, Mathew M. E. Diamond, and A. M. Wing. Active touch sensing. *Philosophical transactions of the Royal Society of London. Series B, Biological sciences*, 366:2989–95, 11 2011.

[7] V. Hayward. *A Brief Overview of the Human Somatosensory System*, pages 29–48. Springer International Publishing, Cham, 2018.

[8] K. Friston. Prediction, perception and agency. *International Journal of Psychophysiology*, 83(2):248–252, 2012.

[9] A. Takagi, F. Usai, G. Ganesh, V. Sanguineti, and E. Burdet. Haptic communication between humans is tuned by the hard or soft mechanics of interaction. *PLOS Computational Biology*, 14(3):1–17, 03 2018.

[10] P. Song, Y. Yu, and X. Zhang. Impedance control of robots: An overview. In *2017 2nd International Conference on Cybernetics, Robotics and Control (CRC)*, pages 51–55, 2017.

[11] C. Liu, L. Sharan, E. H. Adelson, and R. Rosenholtz. Exploring features in a bayesian framework for material recognition. In *2010 IEEE Computer Society Conference on Computer Vision and Pattern Recognition*, pages 239–246, 2010.

[12] D. Kobayashi, N. Yata, and Y. Manabe. Acquisition of image features for material perception from fine-tuned convolutional neural networks. In *2016 International Joint Conference on Neural Networks (IJCNN)*, pages 545–550, 2016.

[13] R. W. Fleming. Visual perception of materials and their properties. *Vision Research*, 94:62 – 75, 2014.

[14] R. Dahiya, N. Yogeswaran, F. Liu, L. Manjakkal, E. Burdet, V. Hayward, and H. Jörntell. Large-area soft e-skin: The challenges beyond sensor designs. *Proceedings of the IEEE*, 107(10):2016–2033, 2019.

[15] P. Dallaire, Philippe Giguère, Daniel Émond, and Brahim Chaib-draa. Autonomous tactile perception: A combined improved sensing and bayesian nonparametric approach. *Robotics and Autonomous Systems*, 62(4):422 – 435, 2014.

[16] C. M. Oddo, M. Controzzi, L. Beccai, C. Cipriani, and M. C. Carrozza. Roughness encoding for discrimination of surfaces in artificial active-touch. *IEEE Transactions on Robotics*, 27(3):522–533, 2011.

[17] S. Takamuku, G. Gomez, Koh Hosoda, and R. Pfeifer. Haptic discrimination of material properties by a robotic hand. In *2007 IEEE 6th International Conference on Development and Learning*, pages 1–6, 2007.

[18] J. Hoelscher, J. Peters, and T. Hermans. Evaluation of tactile feature extraction for interactive object recognition. In *2015 IEEE-RAS 15th International Conference on Humanoid Robots (Humanoids)*, pages 310–317, 2015.

[19] N. F. Lepora, U. Martinez-Hernandez, H. Barron-Gonzalez, M. Evans, G. Metta, and T. J. Prescott. Embodied hyperacuity from bayesian perception: Shape and position discrimination with an icub fingertip sensor. In *2012 IEEE/RSJ International Conference on Intelligent Robots and Systems*, pages 4638–4643, 2012.

[20] N. F. Lepora, U. Martinez-Hernandez, and T. J. Prescott. Active touch for robust perception under position uncertainty. In *2013 IEEE International Conference on Robotics and Automation*, pages 3020–3025, 2013.

[21] U. Martinez-Hernandez, T. J. Dodd, and T. J. Prescott. Feeling the shape: Active exploration behaviors for object recognition with a robotic hand. *IEEE Transactions on Systems, Man, and Cybernetics: Systems*, 48(12):2339–2348, 2018.

[22] U. Martinez-Hernandez, Tony J. Dodd, Mathew H. Evans, Tony J. Prescott, and Nathan F. Lepora. Active sensorimotor control for tactile exploration. *Robotics and Autonomous Systems*, 87:15 – 27, 2017.

[23] Z. Yi, R. Calandra, F. Veiga, H. van Hoof, T. Hermans, Y. Zhang, and J. Peters. Active tactile object exploration with gaussian processes. In *2016 IEEE/RSJ International Conference on Intelligent Robots and Systems (IROS)*, pages 4925–4930, 2016.

[24] T. Matsubara and K. Shibata. Active tactile exploration with uncertainty and travel cost for fast shape estimation of unknown objects. *Robotics and Autonomous Systems*, 91:314 – 326, 2017.

[25] Z. Pezzementi, E. Plaku, C. Reyda, and G. D. Hager. Tactile-object recognition from appearance information. *IEEE Transactions on Robotics*, 27(3):473–487, 2011.

[26] H. Mohammadi and H. Richter. Robust tracking/impedance control: Application to prosthetics. In *2015 American Control Conference (ACC)*, pages 2673–2678, 2015.

[27] A. M. Khan, D. Yun, M. A. Ali, J. Han, K. Shin, and C. Han. Adaptive impedance control for upper limb assist exoskeleton. In *2015 IEEE International Conference on Robotics and Automation (ICRA)*, pages 4359–4366, 2015.

[28] J. W. Sensinger and R. F. f. Weir. User-modulated impedance control of a prosthetic elbow in unconstrained, perturbed motion. *IEEE Transactions on Biomedical Engineering*, 55(3):1043–1055, 2008.

[29] Y. Li, G. Ganesh, N. Jarrassé, S. Haddadin, A. Albu-Schaeffer, and E. Burdet. Force, impedance, and trajectory learning for contact tooling and haptic identification. *IEEE Transactions on Robotics*, 34(5):1170–1182, 2018.

[30] N. Sornkarn, M. Howard, and T. Nanayakkara. Internal impedance control helps information gain in embodied perception. In *2014 IEEE International Conference on Robotics and Automation (ICRA)*, pages 6685–6690, 2014.

[31] N. Sornkarn, P. Dasgupta, and T. Nanayakkara. Morphological computation of haptic perception of a controllable stiffness probe. *PLOS ONE*, 11(6):1–21, 06 2016.

[32] E. Burdet, R. Osu, D. W. Franklin, T. E Milner, H. Gomi, and M. Kawato. The central nervous system stabilizes unstable dynamics by learning optimal impedance. *Nature*, 414:446–449, 2001.

[33] R. C. Oldfield. The assessment and analysis of handedness: The Edinburgh inventory. *Neuropsychologia*, 9(1):97–113, 1971.

[34] A. Melendez-Calderon, L. Bagutti, B. Pedrono, and E. Burdet. Hi5: A versatile dual-wrist device to study human-human interaction and bimanual control. *2011 IEEE International Conference on Intelligent Robots and Systems*, pages 2578–2583, 2011.

[35] C. D. Takahashi, R. A. Scheidt, and D. J. Reinkensmeyer. Impedance control and internal model formation when reaching in a randomly varying dynamical environment. *Journal of Neurophysiology*, 86(2):1047–1051, 2001.

[36] N. Hogan. Adaptive control of mechanical impedance by coactivation of antagonist muscles. *IEEE Transactions on Automatic Control*, 29(8):681–690, 1984.

[37] F. Lacquaniti, M. Carrozzo, and N. A. Borghese. Time-varying mechanical behavior of multijointed arm in man. *Journal of Neurophysiology*, 69(5):1443–1464, 1993.

[38] R. Pfeifer, M. Lungarella, and F. Iida. Self-organization, embodiment, and biologically inspired robotics. *Science*, 318:1088–1093, 2007.

[39] S. A. Abad, N. Herzig, S. M. H. Sadati, and T. Nanayakkara. Significance of the compliance of the joints on the dynamic slip resistance of a bioinspired hoof. *IEEE Transactions on Robotics*, 35(6):1450–1463, 2019.

[40] H. B. Helbig and M. O. Ernst. Optimal integration of shape information from vision and touch. *Experimental Brain Research*, 179(4):595–606, 2007.

[41] G. Orbán and D. M. Wolpert. Representations of uncertainty in sensorimotor control. *Current Opinion in Neurobiology*, 21(4):629–635, 2011.

[42] S. J. Blakemore, C. D. Frith, and D. M. Wolpert. Spatio-temporal prediction modulates the perception of self-produced stimuli. *Journal of Cognitive Neuroscience*, 11(5):551–559, 1999.

[43] D. W. Franklin and D. M. Wolpert. Specificity of reflex adaptation for task-relevant variability. *Journal of Neuroscience*, 28(52):14165–14175, 2008.

[44] J. B. Heald, D. W. Franklin, and D.M. Wolpert. Increasing muscle co-contraction speeds up internal model acquisition during dynamic motor learning. *Scientific Reports*, 8(1):1–11, 2018.

[45] A. Takagi, G. Ganesh, T. Yoshioka, M. Kawato, and E. Burdet. Physically interacting individuals estimate the partner's goal to enhance their movements. *Nature Human Behaviour*, 1(3), 2017.

[46] A. Takagi, F. Usai, G. Ganesh, V. Sanguineti, and E. Burdet. Haptic communication between humans is tuned by the hard or soft mechanics of interaction. *PLoS Computational Biology*, 14(3):1–17, 2018.

[47] K. A. Thoroughman and R. Shadmehr. Electromyographic correlates of learning an internal model of reaching movements. *Journal of Neuroscience*, 19(19):8573–8588, 1999.

[48] D. W. Franklin, E. Burdet, K. Peng Tee, R. Osu, C.-M. Chew, T. E. Milner, and M. Kawato. CNS learns stable, accurate, and efficient movements using a simple algorithm. *Journal of Neuroscience*, 28(44):11165–11173, 2008.

[49] D. W. Franklin, R. Osu, E. Burdet, M. Kawato, and T. E. Milner. Adaptation to stable and unstable dynamics achieved by combined impedance control and inverse dynamics model. *Journal of Neurophysiology*, 90(5):3270–3282, 2003.

[50] D. J. Herzfeld, P. A. Vaswani, M. K. Marko, and R. Shadmehr. A memory of errors in sensorimotor learning. *Science*, 345(6202):1349–1354, 2014.

[51] K. Takiyama, M. Hirashima, and D. Nozaki. Prospective errors determine motor learning. *Nature Communications*, 6:1–12, 2015.

[52] C. M. Harris and D. M. Wolpert. Signal-dependent noise determines motor planning. *Nature*, 394(6695):780–784, 1998.

[53] E. Todorov and M. I. Jordan. Optimal feedback control as a theory of motor coordination. *Nature Neuroscience*, 5(11):1226–1235, 2002.

[54] C. Wang, Y. Xiao, E. Burdet, J. Gordon, and N. Schweighofer. The duration of reaching movement is longer than predicted by minimum variance. *Journal of Neurophysiology*, 116(5):2342–2345, 2016.

[55] W. L. Nelson. Physical principles for economies of skilled movements. *Biological Cybernetics*, 46:135–147, 1983.

[56] E.A. Theodorou, J. Buchli, and S. Schaal. A generalized path integral control approach to reinforcement learning. *Journal of Machine Learning Research*, 11:3137–3181, 2010.

[57] B. Li, Y. Shi, A. Fontecchio, and Y. Visell. Highly Compliant Tactile Sensing Array. *IEEE Transaction on Biomedical Engineering*, 65(3):687–697, 2018.

[58] T. Salmi, J.M. Ahola, T. Heikkilä, P. Kilpeläinen, and T. Malm. Human-robot collaboration and sensor-based robots in industrial applications and construction. In *Robotic Building*, pages 25–52. Springer, 2018.

[59] A. Sawers and L.H. Ting. Perspectives on human-human sensorimotor interactions for the design of rehabilitation robots. *Journal of Neuroengineering and Rehabilitation*, 11(1):142, 2014.

[60] A. Takagi, M. Hirashima, D. Nozaki, and E. Burdet. Individuals physically interacting in a group rapidly coordinate their movement by estimating the collective goal. *eLife*, 8:1–19, 2019.

[61] G. Carboni, X. Cheng, T. Nanayakkara, A. Takagi, and E. Burdet. The nervous system can improve the visuo-haptic perception by learning optimal muscle cocontraction. submitted:1–18, 2021.